Defining cell type-specific immune responses in a mouse model of allergic contact dermatitis by single-cell transcriptomics

Youxi Liu[1,*], Meimei Yin[1,*], Xiaoting Mao[2,*], Shuai Wu[4,*], Shuangping Wei[2,3], Shujun Heng[1], Yichun Yang[1], Jinwen Huang[6], Zhuolin Guo[5], Chuan Li[2], Chao Ji[6], Liu Hu[2, #], Wenjie Liu[1, #], Ling-juan Zhang[1, # ,δ]

Affiliations:

[1]State Key Laboratory of Cellular Stress Biology, School of Pharmaceutical Sciences, Xiamen University, Xiamen, China

[2]Zhejiang Yangshengtang Institute of Natural Medication Co., Ltd., Hangzhou, China

[3]Yang Sheng Tang (Anji) Cosmetics Co., Ltd., Zhejiang, China

[4]State Key Laboratory of Cellular Stress Biology, School of Life Sciences, Xiamen University, Xiamen, Fujian 350005, China

[5]Department of Dermatology, Shanghai Tenth People's Hospital, Tongji University School of Medicine; Shanghai, China

[6]Department of Dermatology, The First Affiliated Hospital of Fujian Medical University, Fuzhou, China

* These authors contribute equally to this work

[#] Correspondence: lingjuan.zhang@xmu.edu.cn (L.j.Z); wjliu@xmu.edu.cn (W.j.L); lhu@mail.yst.com.cn (L.H)

[δ] Lead contact: Ling-juan Zhang; lingjuan.zhang@xmu.edu.cn, telephone 086-592-2182453

Abstract

Allergic contact dermatitis (ACD), a prevalent inflammatory skin disease, is elicited upon repeated skin contact with protein-reactive chemicals through a complex and poorly characterized cellular network between immune cells and skin resident cells. Here, single-cell transcriptomic analysis of the murine hapten-elicited model of ACD reveals that upon elicitation of ACD, infiltrated $CD4^+$ or $CD8^+$ lymphocytes were primarily the IFNγ-producing type 1 effector phenotype. In contrast, type 2 cytokines (IL4 and IL13) were dominantly expressed by basophils, IL17A was primarily expressed by δγ T cells, and IL1β was identified as the primary cytokine expressed by activated neutrophils and macrophages. Furthermore, analysis of skin resident cells identified a sub-cluster of dermal fibroblasts with preadipocyte signature as a prominent target for $IFNγ^+$ lymphocytes and dermal source for key T cell chemokines CXCL9/10. IFNγ treatment shifted dermal fibroblasts from collagen-producing to CXCL9/10-producing, which promoted T cell polarization toward the type-1 phenotype through a CXCR3-dependent mechanism. Furthermore, targeted deletion of *Ifngr1* in dermal fibroblasts in mice reduced *Cxcl9/10* expression, dermal infiltration of $CD8^+$ T cell, and alleviated ACD inflammation in mice. Finally, we showed that $IFNγ^+$ $CD8^+$ T cells and CXCL10-producing dermal fibroblasts co-enriched in the dermis of human ACD skin. Together, our results define the cell type-specific immune responses in ACD, and recognize an indispensable role of dermal fibroblasts in shaping the development of type-1 skin inflammation through the IFNGR-CXCR3 signaling circuit during ACD pathogenesis.

Introduction

Allergic contact dermatitis (ACD), one of the most common skin inflammatory diseases, is affecting 15–20% of the world population(Vocanson, Hennino, Rozieres, Poyet, & Nicolas, 2009). It is a delayed-type hypersensitivity reaction triggered by repeated skin contact with protein-reactive chemicals with low molecular weight, such as haptens. A typical hapten-induced ACD reaction involves a sensitization phase, followed by an elicitation phase. In the sensitization phase, high doses of low-molecular-weight haptens (<500 Da) penetrate through the skin stratum corneum and are captured by Langerhans cells and dendritic cells, which process these antigens and present them to naïve T cells in the skin-draining lymph nodes, priming and clonally expanding the hapten-specific T cells systemically (Kaplan, Igyarto, & Gaspari, 2012). In the elicitation phase, skin re-exposure to haptens (even at low doses) triggers the activation of hapten-specific T cells and a cascade of inflammatory reactions, generally, 24 to 72 hours after exposure (Manresa, 2021).

Hapten-triggered innate immune response involves the release of a panel of proinflammatory cytokines and/or chemokines, such as IL1β, TNFα, CXCL9/10, CCL17, and CCL20, which contribute to T cell trafficking to the skin (Dufour et al., 2002; Kaplan et al., 2012; Meller et al., 2007). Most of the T cells are recruited by chemokines in an antigen-non-specific manner, but when the recruited T cells encounter specific antigen, T cells proliferate and are activated locally, initiating the inflammatory cascade and promoting the influx and/or activation of cytotoxic cells ($CD8^+$ T cells and natural killer T cells), mast cells (MCs) and M1-polarized inflammatory macrophages (MACs) (Chai et al., 2022; Dufour et al., 2002; Vocanson et al., 2009). Both $CD4^+$ and $CD8^+$ T cells are involved in inflammatory responses, and $CD8^+$ T cells are considered the main effector cells (Chai et al., 2022; Vocanson et al., 2006). Recruited lymphocytes secrete a panel of inflammatory cytokines, such as IFNγ, IL4, IL13 and IL17, which act on

skin-resident cells such as keratinocytes, upregulating the expression of adhesion molecules and cytokines/chemokines, thereby recruiting more T cells, macrophages, mast cells to the affected site (Kaplan et al., 2012). However, the cell type-specific immune response driving ACD pathology still remains poorly defined.

Dermal fibroblasts (dFBs), the main resident cell type in skin dermis, are highly heterogeneous, and can be classified based on their anatomical location (Huang et al., 2022). By single-cell RNA-seq (scRNA-seq), we have recently classified dFBs into distinct non-adipogenic and adipogenic sub-groups, and defined several dermal adipocyte lineage cells (Sun et al., 2023). The primary function of dFBs is to provide structural support for the skin by producing extracellular matrix (ECM) molecules, such as collagen and proteoglycans (Huang et al., 2022), and emerging new studies have recognized that dFBs also have important innate immune functions. We have shown that adipogenic dFBs fight against bacterial infections by producing antimicrobial peptides (Zhang et al., 2019; Zhang et al., 2021; Zhang et al., 2015). In addition, a recent study identified a dFB subset that is involved in activating cytotoxic $CD8^+$ T cells during vitiligo pathogenesis (Xu et al., 2022). However, how dFBs are involved in the inflammatory circuit with lymphocytes during ACD pathogenesis remains largely unexplored.

In this study, ACD was induced in mice by sequential application of 2,4-dinitrofluorobenzene (DNFB), and this is the most commonly used murine model for ACD (Karsak et al., 2007; Manresa, 2021; T. Miyake et al., 2022). In-depth scRNA-seq analysis was performed to characterize of how cytokines associated with ACD were differentially expressed by various immune or skin resident cells. In addition to immune cells, we performed in-depth analysis of the immune response of dFBs. Furthermore, the interaction between dFBs and T cells was investigated by in vitro and in vivo approaches. Finally, human ACD skin samples were analyzed to validate the clinical relevance of our observations in mice. Results

from this study provide a better understanding of the cell-type specific immune responses underlying ACD pathogenesis, and unravel the previously unknown role of dFBs in shaping the type 1 immune response in ACD.

Results

Characterization of mouse allergic skin immune response by single cell RNA transcriptomic analysis

Mice were first sensitized to hapten by applying high dose of DNFB to dorsal skin, and 6 days after sensitization, ACD was elicited by applying a low dose of DNFB to the ears (Figure 1A) (Manresa, 2021). The development of skin erythema and thickening peaked at ~ 24 hours and lasted until ~60 hours post-treatment (*p.t.*) (Figure 1-figure supplement 1A and B). Histological analyses showed that the skin dermis drastically expanded at 24 hours *p.t.*, and the dermis became heavily infiltrated with mononuclear cells by 60 hours *p.t.* (Figure 1-figure supplement 1C).

To characterize the cell type-specific immune responses in this DNFB-elicited mouse ACD model, we performed scRNA-seq of control and ACD ear skin samples, and identified up to 30 cell clusters (Figure 1B), which were grouped into several cell types, including chondrocytes, dermal fibroblasts, keratinocytes, T cells, myeloid cells (basophils/BFs, mast cells/MCs, macrophages/MACs, neutrophils/NEUs) and other skin resident cells based on marker gene expression shown by bubble (Figure 1C) or tSNE plots (Figure 1-figure supplement 1D). Furthermore, differential cell distribution plots (Figure 1D) showed that lymphocytes and myeloid cells were the main cell types recruited to the skin after elicitation of ACD (Figure 1E).

ACD is an inflammatory skin disease, driven by a complicated cell-cell network mediated by several T

cell-associated cytokines, including Th1 cytokine IFNγ, Th2 cytokines IL4, IL13, and Th17 cytokine IL17 (Howie et al., 1996). In addition, IL10 participates in skewing of the Th2 response in a murine model of ACD (Laouini et al., 2003), and IL1β is induced in ACD and potentiates the immune response from both T cells and resident cells (Terui, Kimura, Fujimura, & Aiba, 2021). First, we confirmed that the expression of these cytokines was significantly elevated in ACD compared to that in the control skin samples (Figure 1f and Figure 1-figure supplement 1E and 1F). scRNA-seq gene expression plots revealed that *Ifng*, *Il17* and *Il10* were primarily expressed by T cell sub-clusters as expected; to our surprise, *Il4* and *Il13* were primarily produced by basophils, and *Il1b* was detected at the highest levels in neutrophils and at intermediate levels in other myeloid cells, including basophils and macrophages (Figure 1G, Figure 1-figure supplement 1G).

T cells are primarily polarized to the IFNγ-producing type-1 inflammatory phenotype in ACD

To further define the T cell-specific immune response in ACD, T cell clusters were re-grouped into eight clusters (Figure 2A), which were defined as $CD4^+$, Treg, $CD8^+$, δγT, NKT, NK/ILC1, and ILC2, based on marker gene expression (Figure 2-figure supplement 1A and B). ACD led to a notable increase in the percentage of $CD4^+$, Treg, $CD8^+$, and NK/ILC1, but not in that of δγT and ILC2 cells (Figure 2B). Furthermore, gene expression plots (Figure 2C-D and Figure 2-figure supplement 1C) showed that *Ifng* was robustly induced in $CD4^+$, $CD8^+$, and NK/ILC1 T cell clusters, whereas *Il10* and *Il17a* were moderately induced only in the Treg and δγT cell clusters, respectively. In contrast, *Il4* was barely detectable in all T cell subsets. The expression of *Ifng*, *Il17a,* and *Il10* aligned well with that of key T cell lineage transcription factors (TFs), including *Tbx21* (for Th1), *Rorc* (for Th17), and *Foxp3* (for Treg), respectively (Figure 2-figure supplement 1C and D).

GO pathway analysis of $CD4^+$ and $CD8^+$ T cell clusters revealed that chemokine signaling and type II interferon signaling pathways were among the top upregulated, and TGFβ and PI3K-Akt-mTOR signaling were among the top downregulated pathways in ACD compared control (Figure 2E). Volcano plot of differentially expressed genes (Figure 2F) showed that *Ifng* and several IFN-JAK-STAT-related genes (including *Ifitm1/2/3* and *Stat1*) were among the top upregulated genes in ACD, and genes with reported inhibitory functions for T cell activation and/or Th1 polarization, including *Fos* (Xiao, Deng, Liu, Ge, & Liu, 2012), *Zfp36* (Moore et al., 2018), and *Klf4* (An et al., 2011), were among the top downregulated genes in ACD, compared to those in the control.

Next, we aimed to validate the expression of IFNγ in $CD4^+$ and $CD8^+$ T cells in ACD. First, a time-dependent increase in *Cd4, Cd8* and *Ifng* transcript levels was observed in the DNFB-elicited ACD skin (Figure 2-figure supplement 1E). FACS analysis (Figure 2G and Figure 2-figure supplement 1G-I) showed that DNFB-elicited ACD resulted in a rapid increase in both $CD4^+$ and $CD8^+$ T cells, in which IFNγ expression was significantly induced, whereas IL4/IL13 and/or IL17 expression was inhibited. Together, these results indicate that T cells are primarily polarized to the IFNγ-producing type-1 inflammatory phenotype in DNFB-elicited ACD.

Basophils are major source of type-2 cytokines in ACD

scRNA-seq analysis of myeloid cell clusters showed that ACD led to an increase of basophils, mast cells, neutrophils, and macrophages (Figure 3A). Violin plot analyses of cytokines across major skin or immune cell types confirmed that *Il4* was primarily expressed by basophils and mast cells, whereas *Il1b* was primarily expressed by neutrophils and macrophages (Figure 3B and Figure 3-figure supplement 1A).

Basophils and mast cells have similar functions and developmental processes, and both cell types

express the high-affinity Fc receptor for IgE (FceR1a), the activation of which triggers degranulation and release of proteases, histamine, and a panel of proinflammatory cytokines (Hamey et al., 2021). Volcano plots of genes expressed by mast cells (*Cd11b*$^{-}$*Cma1*$^{+}$*Fcer1a*$^{+}$) and basophils (*Cd11b*$^{+}$*Mcpt8*$^{+}$*Fcer1a*$^{+}$) showed that, in comparison, basophils expressed higher levels of cytokines/chemokines, such as *Il4*, *Il13*, and *Il6*, and mast cells expressed higher levels of *Ccl2* and *Ccl7* (Figure 3c), revealing their differential immune responses in ACD.

Next, we aimed to validate the involvement of BFs and MCs in the DNFB-elicited type 2 immune response. First, the expression levels of *Mcpt8* (BF marker) and *Cma1* (MC marker) were elevated in a time-dependent manner upon ACD-elicitation (Figure 3D). FACS analysis of BFs and MCs, based on the surface expression of CD11B and FcεR1a (Figure 3E and 3F and Figure 3-figure supplement 1B), showed that ACD triggered a rapid increase in the percentage of IL4/IL13-producing CD11B^{+} FcεR1a^{+} BFs as early as 24 hours post-elicitation. In contrast, there was only a moderate and delayed increase in IL4/IL13-producing CD11B^{-} FcεR1a^{+} MCs after ACD-elicitation (Figure 3E and F). In addition, immunostaining analysis showed that elicitation of ACD led to dermal infiltration of both FcεR1a^{+} TPSB^{-} BFs and FcεR1a^{+} TPSB^{+} MCs, in which Th2 cytokines were primarily co-localized (Figure 3-figure supplement 1C).

Activation of neutrophils and macrophages

Time-dependent induction of Il1b and recruitment of CD68^{+} MAC and Ly6G^{+} NEU (MAC marker) after ACD elicitation was confirmed by qRT-PCR analysis (Figure 3G). Sc-RNAseq revealed that *S100a8/9*, *Il1b*, and *Cxcl2* were among the most highly expressed genes in *Ly6g*$^{+}$ neutrophils (Figure 3-figure supplement 1D), and *Il1b* was among the top inducible genes in *Cd68*$^{+}$ MACs after ACD elicitation (Figure 3H). Interestingly, genes associated with immunosuppressive or M2 MACs (*Cd74*, *H2-Ab*, and *Ccl24*)

were among the most downregulated genes in MACs after ACD elicitation (Figure 3H). Furthermore, GO pathway analysis identified “cellular response to IFNγ” as the top upregulated pathway, and “lipid metabolic” and “actin cytoskeleton organization” as the top downregulated pathways in MACs after elicitation of ACD (Figure 3I). Anti-inflammatory function of M2 MACs is fueled by fatty acid oxidation(Batista-Gonzalez, Vidal, Criollo, & Carreno, 2019), and changes in actin organization and cell shape are hallmarks of MAC activation (McWhorter, Wang, Nguyen, Chung, & Liu, 2013). These results provide insights into the mechanisms underlying myeloid activation in ACD. FACS analysis of NEUs and MACs confirmed that elicitation of ACD led to a time-dependent increase in NEU recruitment and a shift of MACs from a resting (Ly6C^{lo}) to an inflammatory (Ly6C^{hi}) state (Figure 3J-K and Figure 3-figure supplement 1E and F) (Rahman et al., 2017). Together, these data suggest that IL1β may be a key effector molecule executing the proinflammatory function of NEUs and MACs, and that IFNγ may play a role in activating MACs during ACD pathogenesis.

Characterization of the immune response of dermal fibroblasts

Although dermal fibroblasts are the main resident cell type in the skin dermis (Huang et al., 2022), their role in regulating ACD remains largely unexplored. PDGFRA, a well-characterized skin pan-fibroblast marker (Driskell et al., 2013; Lynch & Watt, 2018), was used to identified dFBs, and *Pdgfra*$^{+}$ dFBs were reclustered into seven sub-clusters (r0 to r6) (Figure 4A). According to dFB and/or adipocyte-lineage cell marker gene profiles reported by our or others’ work (Driskell et al., 2013; Joost et al., 2020; Plikus et al., 2021; Schwalie et al., 2018; Sun et al., 2023; Zachara et al., 2022), the dFB sub-clusters are defined as *Mfap5*$^{+}$*Dlk1*$^{+}$*Ly6a*$^{+}$ adipocyte progenitors (AP in r2), *Fmo2*$^{+}$*Ly6a*$^{+}$ adipose regulatory cells (Areg in r6), *Ly6a*$^{+}$*Lpl*$^{+}$*Apoe*$^{+}$*Icam1*$^{+}$ preadipocytes (pAd, in r1 and r5), *Ly6a*^{lo} or *Lrig1*$^{+}$ reticular or papillary dFBs (RET/PAP in r0), and *Ly6a*^{lo}*Trps1*^{hi} peri-follicular dFBs (including dermal papilla

cells, r4) (Figure 4B, Figure 4-figure supplement 1A and B).

Bubble plots and violin plots showed that ACD elicitation led to an increase of the expression of a panel of IFN-inducible genes (*Cxcl9, Cxcl10, Stat1*), accompanied with a loss of the expression of pAd signature genes (*Lpl, Apoe*) and a panel of ECM genes (*Col1a1, Col3a1*) in the r5 pAd cluster (Figure 4C and Figure 4-figure supplement 1C and D). In addition, scenic TF analysis revealed that the dFB_r5 cluster was specifically enriched with several TFs downstream of the interferon pathway (*Stat1, Irf1*, and *Irf7*) (Figure 4D). Furthermore, GO pathway analysis of dFB_r5 cells showed that pathways including response to virus, cellular response to IFNγ, and positive regulation of T cell-mediated cytotoxicity were among the top upregulated pathways, whereas ECM organization was among the top downregulated pathways in ACD compared to control (Figure 4E). Accordingly, volcano gene expression plots of dFB_r5 cluster showed that *Cxcl9, Cxcl10, Ccl2, Stat1,* and other antiviral genes were the top upregulated genes, whereas ECM genes were the top downregulated genes in ACD compared to control (Figure 4F).

Violin plots of major skin and immune cell types showed that inflammatory genes related to the IFNGR pathway (*Stat1*, *Cxcl9*, *Cxcl10*) were expressed at highest levels in the dFB_r5 cluster, whereas *Ifng* and *Cxcr3* (receptor for CXCL9/10 ligands) was mainly expressed by T cells (Figure 4G and Figure 4-figure supplement 1E). qRT-PCR validated the time-dependent induction of chemokines after ACD elicitation (Figure 4-figure supplement 1F). Co-immunostaining analyses showed that $CXCL9^{+}$ or $CXCL10^{+}$ cells co-expressed PDGFRA in the dermis of ACD skin sample (Figure 4H-J and Figure 4-figure supplement 1G), supporting that dFB is the major cell source for CXCL9/10 in ACD. In addition, phosphor-STAT1 (pSTAT1), a key signaling molecule activated by IFNγ, was detected primarily in $PDGFRA^{+}Ly6A^{+}$ pAds located around the lower reticular dermis and dermal fat area (Figure 4-figure supplement 1H and I). Together, we have identified a cluster of dFB with pAd signature as a cellular

source of T cell chemokines CXCL9/10 in ACD, suggesting that dFBs may play a role in the development of type-1 immune response by interacting with T cells.

Interaction between dermal fibroblasts and T cells via the IFNγ-CXCL10-CXCR3 signaling axis

We next aimed to validate the interaction between dFBs and T cells. First, unbiased IFNγ-IFNGR signaling network analysis showed that elicitation of ACD enabled IFNγ production from $CD4^+$/$CD8^+$ or ILC1/NK T cells, acting on the dFB-r5 cluster (Figure 5A).

To define the IFNγ-dependent immune response in dFBs and to determine how dFBs respond differently to IFNγ compared to other T cell-derived cytokines, primary dFBs were stimulated with IFNγ, IL4, or IL17A. Transcriptomic venn diagram analysis showed that IFNγ uniquely upregulated the expression of a large pool of genes, including several antiviral- or IFNγ pathway-related genes (Figure 5B and C). Time course analysis showed that IFNγ treatment robustly induced the expression of *Cxcl9, Cxcl10, Stat1,* and *Ccl2* as early as 8 hours post-treatment, and suppressed the expression of lipogenesis (*Apoe*) and ECM (*Col1a1*) genes in a delayed manner (Figure 5B and Figure 5-figure supplement 1A). These in vitro changes in dFBs highly correlated with the transcriptomic change of the r5_dFB cluster upon ACD elicitation. Additionally, *Cxcr3* was specifically induced in T cells in ACD (Figure 5-figure supplement 1B), suggesting that IFNGR-dependent activation of dFBs may in turn promotes T cell recruitment/activation by producing CXCL9/10, which act on T cells via CXCR3.

Next, to determine whether IFNγ-primed dFBs can directly promote T cell activation through the CXCL9/10-CXCR3 axis, we established an in vitro co-culture system between primary dFBs and naïve lymphocytes (Figure 5E). ELISA confirmed that IFNγ-primed dFBs secreted high level of CXCL10 (Figure 5F), and conditioned medium from unstimulated control or IFNγ-primed dFBs (dFB^{ctrl}-CM or $dFB^{IFNγ}$-CM)

was then added to primary lymphocytes with or without CD3/CD28-antibody costimulation. We found that in the absence of CD3/CD28 antibody, dFB^{IFNγ}-CM significantly enhanced IFNγ production from naïve T cells, and blocking CXCR3 signaling by adding a CXCR3 neutralizing antibody inhibited this effect (Figure 5G). Interestingly, in the presence of CD3/CD28 antibody, we found that compared to blank DMEM, dFB^{ctrl}-CM inhibited IFNγ expression and promoted T cell polarization towards the IL4-producing type-2 phenotype, whereas dFB^{IFNγ}-CM downregulated IL4 expression and restored the ability of stimulated T cells to produce IFNγ (Fig.5H and Figure 5-figure supplement 1C). In addition, the effect dFB^{IFNγ}-CM was partially reversed by adding a CXCR3 neutralizing antibody (Figure 5H and Figure 5-figure supplement 1C). These results indicate that IFNγ-primed dFBs are capable to shift the T1/T2 polarization balance towards type-1 effector phenotype by activating the CXCR3 pathway during T cell activation.

Targeted deletion of *Ifngr* in dermal fibroblasts inhibited the development of type-1 skin inflammation in ACD

To validate the role of IFNGR in activating dFB, we generated tamoxifen (TAM)-inducible fibroblast-specific *Ifngr1* knockout mice by crossing *Ifngr1*$^{flox/flox}$ mice with *Pdgfra*-cre/*ERT* mice (Xu et al., 2022), termed as "*Ifngr1*$^{FB\text{-}iKO}$" mice (Figure 6A). TAM application to *Ifngr1*$^{FB\text{-}iKO}$ mice specifically ablated the expression of *IFNGR1* in PDGFRA^{+} dFBs, but not in other PDGFRA^{-} dermal cells (Figure 6C and Figure 6-figure supplement 1A and B). As a result, DNFB-mediated development of skin eczema (Figure 6D and E), dermal cell infiltration (Figure 6F), induction of *Cxcl9/10, Cxcr3*, *Ifng, Cd8a* and other inflammatory genes (Figure 6G and Figure 6-figure supplement 1C), and dermal infiltration of CD8^{+} T cells (Figure 6H and I) were significantly inhibited in the *Ifngr1*$^{FB\text{-}iKO}$ mice. These results demonstrate that targeted deletion of IFNγ receptor signaling in dermal fibroblasts inhibited the development of type-1 skin inflammation in ACD.

Activation of dermal T cells and fibroblasts in human ACD skin samples

Finally, to determine whether these observations in mice are of human relevance, human ACD skin biopsies were collected for analysis. Co-immunostaining of IFNγ with CD4 and CD8 revealed that numerous $CD8^+$ $IFN\gamma^+$ T cells were present in the dermal micro-vascular structures, which are known to be enriched with mesenchymal stem cells(Russell-Goldman & Murphy, 2020), in ACD skin, but not in healthy control skin (Figure 7A). In addition, within these dermal structures, IFNγ was detected exclusively from $CD8^+$ T cells (Figure 7B). In contrast, infiltration of $CD4^+$ T cells was not observed, suggesting that $CD8^+$ T cells are the major IFNγ-producing cells in the human ACD skin.

We have shown that ACD led to decrease collagen expression in dFBs (Figure 4). To determine how collagen was altered in human ACD, skin sections were subjected to Masson's staining to visualize collagen bundles in blue (Figure 7C). In line with our mouse data, collagen bundles were thinner and disorganized within the dermal micro-vascular structures where immune cells were heavily infiltrated in human ACD skin compared to healthy control skin sections (Figure 7C). In mouse ACD model, we showed that IFNGFR-mediated activation of dFBs promotes the infiltration and activation of $CD8^+$ T cells to skin dermis (Figure 6). Here, co-immunostaining of PDGFRA and CD8 revealed that $CD8^+$ T cells were infiltrated around the $PDGFRA^+$ dermal fibroblasts within the dermal micro-vascular structure in ACD skin (Figure 7D). Furthermore, $PDGFRA^+$ dermal fibroblasts within these micro-vascular structures expressed CXCL10 (Figure 7E and F). This human dFB population correlated with the dFB-r5 cluster we identified in the murine DNFB-elicited ACD skin, in which *CXCL9/10* were strongly induced and collagen genes were inhibited.

Discussion

In contrast to other inflammatory skin diseases, such as atopic dermatitis (mainly involving a Th2 immune response) and psoriasis (mainly involving a Th17 immune response), ACD results from a complex but poorly defined inter-connected network between the Th1, Th2, and Th17 pathways. In this study, we provide a comprehensive single cell analysis of the cellular interaction network of key T cell cytokines and/or chemokines in a DNFB-induced mouse model of ACD. We found that $CD4^+$and $CD8^+$ lymphocytes are primarily polarized towards the IFNγ-producing type 1 effector phenotype. In contrast, type 2 cytokines (IL4 and IL13) are primarily produced by basophils. Interestingly, our study identified a cluster of dermal fibroblasts with pAd signature as a dermal source for key T cell chemokines CXCL9/10. Targeted deletion of *Ifngr1* in dermal fibroblasts reduced DNFB-induced infiltration of $CD8^+$ T cell to the skin, the expression of *Cxcl9, Cxcl10* and *Ifng*, and alleviated the development of ACD in mice. The results unravel a previously unrecognized role of dFBs/pAds in regulating type-1 skin inflammation.

In line with our findings, targeting type-1 immune response has emerged as effective therapeutic approach against allergic skin diseases (Liu et al., 2023; Wongchang et al., 2023; Wu et al., 2021). Interferon signaling, including IFNγ signaling, has been identified as a highly enriched pathway during nickel-induced contact allergy in humans (Wisgrill et al., 2021). Additionally, comparisons between sodium lauryl sulfate-irritated and nickel-sensitized skin samples revealed that nickel-sensitized samples were uniquely enriched with pathways related to T-cell activation, including JAK-STAT signaling, natural killer cell mediated cytotoxicity and T cell receptor signaling (Wisgrill et al., 2021). Furthermore, *Ifng* knockout mice failed to elicit contact hypersensitivity to urushiol (Wakabayashi et al., 2005), supporting that IFNγ plays a pivotal role in ACD pathogenesis.

CXCL9, CXCL10 and interferon-related pathways are recognized as potential major hallmarks that distinguish allergic-induced from irritant-induced skin inflammation (Lefevre et al., 2021). A study

investigating the differential involvement of chemokines in chemical-induced allergic skin responses compared to irritant skin responses showed that CXCL9 and CXCL10 were among the top five chemokines that were uniquely upregulated in hapten-induced skin allergic inflammation but were absent in inflammation triggered by irritants (Meller et al., 2007). *Cxcl10* knockout mice display an impaired contact hypersensitivity response, characterized by reduced inflammatory cell infiltrates in the skin and reduced T cell activation and proliferative response (Dufour et al., 2002). $CD4^+$ and $CD8^+$ T cells showed a dose-dependent migration response to CXCL10 in vitro, and adoptive transfer of CXCL10-primed leukocytes isolated from hapten-sensitized mice increased skin inflammation after hapten challenge in vivo (Meller et al., 2007).

The role of dermal fibroblasts in ACD is poorly understood. Our results identified a cluster of CXCL9/10-producing dFBs/pAds in ACD, and showed that targeted deletion of *Ifngr1* in $PDGFRA^+$ dFB not only reduced DNFB-induced *Cxcl9/10* production but also reduced trafficking of $CD8^+$ T cells to affected skin sites. These results suggest that an inflammatory amplification circuit may exist between T cells and dFBs through the IFNγ–IFNGR and CXCL9/10-CXCR3 signaling network, providing a better understanding of the mechanism of action underlying IFNγ- and/or CXCL9/10-driven allergic skin inflammation. In line with our results, a recent study by Prof. Chen's group revealed the emerging roles of dFBs in the development of autoimmune diseases. They identified a subset of IFNγ-responsive dFBs which are required to recruit and activate $CD8^+$ cytotoxic T cells during the pathogenesis of vitiligo (Xu et al., 2022). In response to paracrine IFNγ signaling, dFBs orchestrate autoimmune $CD8^+$ T cells through secreted chemokines, including CXCL9 and CXCL10. Furthermore, the authors showed that anatomically distinct fibroblast subsets with differential IFNγ responses are the key determinants of body-level patterns of lesions in vitiligo, highlighting dFB subpopulations as therapeutic targets for vitiligo and other

autoimmune diseases. While our results reveal that the cellular interaction between lymphocytes and dFBs promotes ACD pathology, a recent study shows that the innate δγ T cells interact with $CD8^+$ T cells through the IFNγ – IFNGR pathway to restrain the proliferative and effector potential of $CD8^+$ T cells (Munoz-Ruiz et al., 2023), suggesting that activation of IFNGR signaling may either promote or inhibit type-1 effector immune response in a cell-type specific manner.

Infiltration of basophils into inflammatory sites has been demonstrated in several allergic diseases, including atopic dermatitis, allergic rhinitis and asthma (K. Miyake & Karasuyama, 2017); however, basophils are often regarded as minor relatives of mast cells and have long been neglected in immunological studies. Using several independent approaches, including scRNA-seq, FACS and immunostaining, we showed that basophils rapidly infiltrated the skin dermis and were the primary source of Th2 cytokines (IL4 and IL13) in DNFB-elicited ACD skin. In line with our report, a recently published scRNA-seq study of an ovalbumin (OVA)-sensitized murine skin model also unexpectedly found that mast cells/basophils, rather than T cells, are the major source of IL4 and IL13 (Xu et al., 2022). Another recent study showed that basophil-mediated type-2 immune response is mediated by IL3-produced by T cells in the hapten-induced ACD mouse model (Hachem et al., 2023). Future studies investigating cellular interactions between basophils and dFBs will advance our understanding of the basophil chemotaxis mechanism and the role of basophils in skin allergic inflammation.

Taken together, our findings highlight a central role of type-1 immune response in driving ACD-like skin inflammation in both mice and human, and indicate that dermal fibroblasts are not just structural cells but also play a viscous role in amplifying type-1 inflammation in skin dermis. The interaction between T cells and dFBs may be potential therapeutic targets for allergic skin reactions. Furthermore, because IFNγ plays a central role in host defense, anti-tumor immunity, and autoimmunity (Kwon, 2018; Pollard, Cauvi,

Toomey, Morris, & Kono, 2013), results from our study suggest that tissue-resident fibroblasts may play a role in shaping the development of type-1 immune response in other diseases, such as infectious diseases (such as herpes simplex), cancer, and autoimmune disorders, such as psoriasis, rheumatoid arthritis and systemic lupus erythematosus.

Materials and methods

Animals and animal cares

ICR or C57BL/6 mice used in this study were purchased from GemPharmatech (Nanjing, China), then bred and maintained in standard pathogen free (SPF) environment of the Laboratory Animal Center in Xiamen University. C57BL/6J-*Ifngr1*$^{flox/flox}$ (Stock No: T009548) was originally purchased from GemPharmatech (Nanjing, China) and *Pdgfra-creERT* (Stock No: 018280) mice were originally purchased from Jackson laboratory (Bar Harbor, ME, USA). The tamoxifen-inducible *Ifngr1* conditional knockout mice were generated by breeding *Ifngr1*$^{flox/flox}$ with *Pdgfra-cre/ERT* mice. *Pdgfra-creERT*; *Ifngr1*$^{flox/flox}$ male mice (n=4/group) were daily administrated intraperitoneally with tamoxifen (Sigma-Aldrich, St. Louis, MO, USA) solution (20 mg/mL stock solution dissolved in corn oil (Aladdin, Shanghai, China) at 75 mg/kg body weight from post-sensitization day 3 to day 8. All mice were bred and maintained in standard pathogen free environment of the Laboratory Animal Center in Xiamen University, and all animal experiments were approved by the Animal Care and Use Committee of Xiamen University. (protocol code XMULAC20190090).

DNFB-induced mouse model of ACD

DNFB-induced ACD mouse model was carried out according to published protocol(Manresa, 2021). For sensitization, the dorsal skin of 7~8 weeks old male ICR mice (n=8) was first painted with 25 μL 1.0% DNFB (dissolved in 4:1 mixture of acetone and olive oil) (Xilongs, Shenzhen, China). Six days after

sensitization, to elicit ACD, 20 μL 0.2% DNFB was painted to each ear, and ear skin samples were collected at 24 hours or 60 hours post-elicitation for analysis. For treatments, 250 μL undiluted birch sap extract (BSE) was topically applied to ear skin from 12 hours post-elicitation, 3 times a day, and ear skin samples were collected at 60 hours post-elicitation. 1% Hydrocortisone (HC) ointment (Aveeno, Johnson & Johnson, Maidenhead, Berkshire, UK) was used as the positive group, and dH_2O was used as the vehicle control.

Human skin sample collection and analysis

Fresh adult human full thickness skin biopsies, from age and sex matched healthy and ACD donors were collected by the department of dermatology at the First Affiliated Hospital of Fujian Medical University. ACD disorder was diagnosed based on their clinical appearance, history and treatment history. All ACD samples analyzed in this study were consistent with clinical and pathological criteria for ACD patients. All sample acquisitions were approved and regulated by Medical Ethics Committee of the First Affiliated Hospital of Fujian Medical University (reference number No. 2020[146]). The informed consent was obtained from all subjects prior to surgical procedures. Upon collection, these samples were directly fixed with paraformaldehyde (PFA) then proceed for paraffin embedding for histological or immunofluorescent analyses.

Single cell RNA library preparation, sequencing and data process

Ear skin biopsies were collected from control or DNFB-elicited skin, and skin biopsies were minced and digested with collagenase D and DNase1 to isolate single skin cells as previously described (Sun et al., 2023). Dead cells were removed using DeadCell Removal kit (Miltenyi Biotic,130-090-101) according to manufacturer’s instruction. Live cells were counted using a hemocytometer and resuspended in 2% BSA at a concentration of 3,000 cells/uL. All three samples were loaded on a 10x

Genomics GemCode Single-cell instrument that generates single-cell Gel Bead-In-EMlusion (GEMs. Barcoded, full-length cDNAs were reverse-transcribed from polyadenylated mRNA. Silane magnetic beads were used to remove leftover biochemical reagents and primers from post GEM reaction mixture. Next, libraries were generated and sequenced from the cDNAs with Chromium Next GEM Single Cell 3' Reagent Kits v 2. cDNA libraries were sequenced on an Illumina Novaseq6000 platform (Illumina). The raw sequencing data was demultiplexed and aligned to the reference genome mm10-1.2.0 using Cell Ranger v3.0.2 pipiline(10x Genomics). The generated raw gene expression matrix was converted into Seurat objects using the R package Seurat v2.0. To remove doublets and poor-quality cells, we utilized the following procedures to control for cell quality: >200 genes/cell, <5000 genes/cell; >25,000 unique molecular identifiers(UMIs) ; and <8% mitochondrial gene expression. Low quality cells and outliers were discarded, and only ~ 18,241 viable cells were used for downstream analysis. These included ~9,871 cells – control; ~8,370 cells – DNFB-elicited ACD. Unsupervised clustering and gene expression were visualized with the Seurat 2.0 on R studio, and assignment of cell clusters was based on expression of validated marker genes. Single cell RNA libraries construction, sequencing and bioinformatic analysis was assisted by GENE DENOVO Inc (Guangzhou, China).

Cell-chat signaling network analysis

R package CellChat 1.3.0(Jin et al., 2021) was used to evaluate the potential cell-cell communication between dFB subclusters and other cell types, especially immune cells, during ACD pathogenesis. The scRNA-seq data was imported to implement CellChat platform in R software. The process includes projecting the gene expression data onto protein-protein interaction (PPI) network, then assigning a probability value to infer biological cell-cell communication network, and calculating the centrality indicator

of interacting network to identify the role / contribution of each cell population in distinct signaling pathways. The number and strength of identified cell-cell communication is displayed through hierarchical graphs, circle charts, heatmaps, etc. to visualize single or multiple signaling pathways.

Flow cytometry analysis and cell sorting

FACS procedure of dermal fibroblasts and immune cells was modified from previously established or reported methods (Sun et al., 2023; Zhang et al., 2019). Skin tissues were digested with collagenase D (Sigma-Aldrich, St. Louis, MO, USA) and Dnase 1 (Solarbio, Beijing, China) to prepare single cell suspension. Cell mixture was then filtered through 30 μm filter and treated with red blood cell lysis buffer. For analyzing cytokine expression in skin-derived T cells, isolated skin cells were first cultured in vitro in the presence of PMA (50ng/ml) (yeasen, Shanghai, China) and Ionomycin (500ng/ml) (Sigma-Aldrich, St. Louis, MO, USA) for 2 hours and Golgi-plug (1:1000) (BD biosciences, California, USA) for additional 1 hour prior to being subjected to FACS analysis. Briefly, freshly isolated mouse skin cells were first stained with zombie violet viability dye (BioLegend, #423114) to label dead cells. Cells were then blocked with anti-mouse CD16/32 (eBioscience, #14016185), followed by staining with an antibody cocktail for T cells containing PECy7-CD45 (BioLegend, #147704), PerCP-Cy5.5-CD8 (eBioscience, #45-0081-82), and APC-CD4 (BioLegend, #100516), an antibody cocktail for basophils and mast cells containing PECy7-CD11B (Biolegend, #101216), PE-FcεR1α (BioLegend, #134307) and APC-c-kit (BioLegend, #135108), or an antibody cocktail for immune cells containing FITC-Ly6G (eBioscience, #11593182), PE-F4/80 (eBioscience, #12480182), APC-CD11C (BioLegend, #117310), AF700-MHCII (eBioscience, #56532182), PerCP-Cy5.5-Ly6C (BioLegend, #128012), PECy7-CD11B (Biolegend, #101216), APC-Cy7-CD3 (BioLegend, #100222). To stain intracellular proteins in immune cells, stained cells were then fixed and permeabilized using the intracellular fixation and permeabilization buffer set (eBioscience,

#00-8333-56) and stained by FITC-IL4 (BioLegend, #504109), FITC-IL13 (eBioscience, #53-7133-82), AF700-IFNG (BioLegend, #505824), PE-IL17A (eBioscience, #12-7177-81). FACS analysis for protein expression of each cell marker was performed by the Thermo Attune NxT machine and analyzed by FlowJo V10 software. Dead cells stained positive with zombie violet dye were excluded from the analyses.

Histology, collagen trichrome staining, toluidine blue and immunohistochemistry (IHC)

Staining was performed on either paraffin sections or frozen sections as described previously(Zhang et al., 2019; Zhang et al., 2021). Histology was assessed by Hematoxylin and Eosin (HE) staining solutions, and collagen was stained by the Masson's Trichrome Stain Kit (Solarbio, Beijing, China). For IHC, fixed sections were permeabilized with 0.1% saponin (Sigma-Aldrich, St. Louis, MO, USA) and blocked in 5% BSA, and blocked sections were incubated with primary antibodies at 4°C overnight followed by appropriate 488-, Cy5 or Cy3-coupled secondary antibodies in the dark for 4 hours at 4°C. Finally, sections were mounted by ProLong Gold Antifade Mountant with DAPI (Thermo Fisher Scientific, Cleveland, OH, USA). All images were taken with Aperio VERSA Brightfield, Fluorescence Digital Pathology Scanner or Leica TCS SP8 White Light Laser Confocal Microscope, and processed by photoshop and/or Aperio ImageScope software (Leica Biosystems, Nußloch, Germany).

Quantitative reverse transcription-quantitative PCR (qRT-PCR) analyses

Total cellular RNA was extracted using the RNAExpress Total RNA Kit (NCM , Suzhou, China) and 500 ng of RNA was reverse transcribed to cDNA using HiScript III Q RT SuperMix kit (Vazyme, Nanjing, China). Quantitative, realtime PCR was performed on the Qtower real time system (Analytikjena, Ilmenau OT Langewiesen • Germany) using SYBR Green Mix (Bimake, Houston, Texas, USA). All of the primers

used with SYBR green were designed to span at least one exon to minimize the possibility of nonspecific amplification from the genomic DNA. The expression of *Tbp* gene (TATA-Box Binding Protein) was used as a housekeeping gene to normalize data for the expression of mouse genes. Specific primer sequences are shown in tables S1.

Bulk RNA sequencing and bioinformatic analysis:

Total cellular RNA were extracted using TRIzol reagent (Sigma,T9424) and RNAExpress Total RNA Kit (NCM, M050). RNA quality was analyzed by bioanalyzer and RNA samples with RIN value > 7 were used for sequencing. Next generation sequencing library preparations were constructed according to the manufacturer's protocol (NEBNext Ultra RNA Library Prep Kit for Illumina). The poly(A) mRNA isolation was performed using NEBNext Poly(A) mRNA Magnetic Isolation Module (NEB). The mRNA fragmentation and priming were performed using NEBNext First Strand Synthesis Reaction Buffer and NEBNext Random Primers. First strand cDNA was synthesized using ProtoScript II Reverse Transcriptase and the second-strand cDNA was synthesized using Second Strand Synthesis Enzyme Mix. The purified double-stranded cDNA was then treated with End Prep Enzyme Mix to repair both ends and add a dA-tailing in one reaction, followed by a T-A ligation to add adaptors to both ends. Size selection of Adaptor-ligated DNA was then performed using AxyPrep Mag PCR Clean-up (Axygen), and fragments of ~420bp (with the approximate insert size of 300 bp) were recovered. Each sample was then amplified by PCR. The PCR products were cleaned up using AxyPrep Mag PCR Clean-up (Axygen), validated using an Agilent 2100 Bioanalyzer (Agilent Technologies), and quantified by Qubit 2.0 Fluorometer (Invitrogen). Then libraries with different indexs were multiplexed and loaded on an Illumina Navoseq instrument for sequencing using a 2x150 paired-end (PE) configuration according to manufacturer's instructions. The sequences were processed and analyzed by GENEWIZ. Venn diagrams between gene sets were made

by BioVenn. KEGG and gene ontology (GO) pathway analysis for differentially expressed genes and correlation analysis between single cell RNA-seq with bulk RNA-seq were performed by R package clusterProfile 3.12.0.

Cell extract preparation and ELISA assay

Skin biopsies were lysed in a lysis buffer supplemented with completed proteinase inhibitor cocktail (Apexbio, Houston, USA) to maximally preserve protein modifications as described previously (Zhang et al., 2021). Lysates were homogenized by sonication using digital sonifier FS- 350T (Sxsonic, Shanghai, China) followed by centrifugation to remove DNA and cell debris. Protein concentrations were measured by BCA protein assay kit. Protein lysates were subjected to enzyme-linked immunosorbent assay (ELISA) using mouse DuoSet® ELISA commercial kits (R&D Systems, Minneapolis, MN, USA), following manufacturer instructions.

Primary culture of mouse dermal fibroblasts

Primary mouse dermal fibroblasts were isolated from mouse skin as described previously (Zhang et al., 2019; Zhang et al., 2021). Isolated cells were plated on culture dish in growth medium (DMEM supplemented with 10% FBS and antibiotics/antimycotics) in a humidified incubator at 5% CO_2 and 37°C under sterile conditions. Cells from the first passage were replated at 1 x 10^5/mL for in vitro assays. For in vitro IFNγ treatment, dFBs were treated with either recombinant mouse IFNγ (5 ng/ml, R&D Systems, Minneapolis, MN, USA) for 8 or 24 hours before being subjected to qRT-PCR or ELISA analysis.

Dermal fibroblasts and T cells co-culture

To collected IFNγ-primed dFB conditioned medium (CM), primary dFBs were treated with IFNγ (5 ng/ml, R&D Systems) or PBS control for 2 hours, cells were washed twice with PBS then replenished with

fresh medium without IFNγ for additional 48 hours, and CM was collected for the subsequent co-culture experiment with T cells. Primary lymphocytes isolated from skin draining lymph nodes from adult C57BL/6 mice were cultured on plates precoated with anti-mouse α-CD3 (3 μg/ml, Biolegend, #100340) and anti-mouse α-CD28 (3 μg/ml, Biolegend, #102116) in RPMI medium supplemented with 10% FBS with or without dFB-CM. After 4 days, medium was collected for ELISA analysis. To neutralize CXCR3, T cells were pretreated with anti-CXCR3 neutralizing antibody (10 ug/ml, Biolegend, #126526) or control IgG antibody (10 ug/ml, Biolegend, #400902) for 30 mins before adding dFB-CM. For treatments, T cells were pretreated with 5% undiluted BSE for 30mins before adding dFB-CM and 5% dH_2O was used as the vehicle control.

Statistical analysis

Experiments were repeated at least 3 times with similar results and were statistically analyzed by GraphPad Prism 8 software. For experiments with two groups, statistical significance was determined using Student's unpaired two-tailed t-test. For experiments with more than two groups, one-way ANOVA multiple comparison test was performed as indicated in the legend. A P value of <0.05 was considered statistically significant (*P<0.05, **P<0.01, ***P<0.001, ****P<0.0001).

Acknowledgements

We thank the flow-cytometry and microscopic core facility at Xiamen University for aiding with flow-cytometry analysis and imaging studies.

Funding

Funder	Grant reference number	Author

National Key Research and Development Program of China	2023YFC2508100	Lingjuan Zhang
National Natural Science Foundation of China	82373879, 81971551	Lingjuan Zhang
National Key Research and Development Program of China	2020YFA0112901	Lingjuan Zhang Wenjie Liu

The funders had no role in study design, data collection and interpretation, or the decision to submit the work for publication.

Author contributions

Conceptualization, Y.L., M.Y., S.Wang, S.Wei, L.H., W.L. and L.Z.; methodology, Y.L., M.Y., S.Wang, S.Wei, S.Wu, S.H., W.L., and L.Z.; investigation, Y.L., M.Y., S.Wu, S.H., Y.Y., Z.G., and W.L.; resources, S.Wang, S.Wei, J.H., C.J., and L.H.; data curation, Y.L., M.Y., S.Wu, W.L., and L.Z.; writing-original draft, Y.L., M.Y., W.L., and L.Z.; writing-review and editing, Y.L., M.Y., S.Wang, S.Wei, L.H., W.L.,and L.Z.; supervision, L.Z.

Supplementary files

- **MDAR checklist**
- **Supplementary Table S1.** List of gene primers used for RT-qPCR

Data availability

The accession numbers for the raw data files of the scRNA-seq analyses reported in this paper are deposited in the GEO database under accession codes: GSE224848. All data were analysed with commonly used open-source software programs and packages as detailed in the Materials and methods

section.

The following dataset was generated:

Author(s)	Year	Dataset title	Database and Identifier
Zhang, L.j.	2023	Defining Cell Type-specific Immune Responses in Allergic Contact Dermatitis by Single-cell Transcriptomics	NCBI GEO database under accession codes: GSE224848

References

An, J., Golech, S., Klaewsongkram, J., Zhang, Y., Subedi, K., Huston, G. E., . . . Weng, N. (2011). Kruppel-like factor 4 (KLF4) directly regulates proliferation in thymocyte development and IL-17 expression during Th17 differentiation. *FASEB J, 25*(10), 3634-3645. doi:10.1096/fj.11-186924

Batista-Gonzalez, A., Vidal, R., Criollo, A., & Carreno, L. J. (2019). New Insights on the Role of Lipid Metabolism in the Metabolic Reprogramming of Macrophages. *Front Immunol, 10*, 2993. doi:10.3389/fimmu.2019.02993

Chai, W., Zhang, X., Lin, M., Chen, Z., Wang, X., Wang, C., . . . Gui, J. (2022). Allergic rhinitis, allergic contact dermatitis and disease comorbidity belong to separate entities with distinct composition of T-cell subsets, cytokines, immunoglobulins and autoantibodies. *Allergy Asthma Clin Immunol, 18*(1), 10. doi:10.1186/s13223-022-00646-6

Driskell, R. R., Lichtenberger, B. M., Hoste, E., Kretzschmar, K., Simons, B. D., Charalambous, M., . . . Watt, F. M. (2013). Distinct fibroblast lineages determine dermal architecture in skin development and repair. *Nature, 504*(7479), 277-+. doi:10.1038/nature12783

558 Dufour, J. H., Dziejman, M., Liu, M. T., Leung, J. H., Lane, T. E., & Luster, A. D. (2002). IFN-gamma-inducible
559 protein 10 (IP-10; CXCL10)-deficient mice reveal a role for IP-10 in effector T cell generation and
560 trafficking. *J Immunol, 168*(7), 3195-3204. doi:10.4049/jimmunol.168.7.3195
561 Hachem, C. E., Marschall, P., Hener, P., Karnam, A., Bonam, S. R., Meyer, P., . . . Li, M. (2023). IL-3 produced
562 by T cells is crucial for basophil extravasation in hapten-induced allergic contact dermatitis. *Front*
563 *Immunol, 14*, 1151468. doi:10.3389/fimmu.2023.1151468
564 Hamey, F. K., Lau, W. W. Y., Kucinski, I., Wang, X., Diamanti, E., Wilson, N. K., . . . Dahlin, J. S. (2021).
565 Single-cell molecular profiling provides a high-resolution map of basophil and mast cell development.
566 *Allergy, 76*(6), 1731-1742. doi:10.1111/all.14633
567 Howie, S. E., Aldridge, R. D., McVittie, E., Forsey, R. J., Sands, C., & Hunter, J. A. (1996). Epidermal
568 keratinocyte production of interferon-gamma immunoreactive protein and mRNA is an early event in
569 allergic contact dermatitis. *J Invest Dermatol, 106*(6), 1218-1223. doi:10.1111/1523-1747.ep12348507
570 Huang, J., Heng, S., Zhang, W., Liu, Y., Xia, T., Ji, C., & Zhang, L. J. (2022). Dermal Extracellular Matrix
571 molecules in skin development, homeostasis, wound regeneration and diseases. *Semin Cell Dev Biol*
572 *S1084-9521*(22), 00064-00067. doi:10.1016/j.semcdb.2022.02.027
573 Jin, S., Guerrero-Juarez, C. F., Zhang, L., Chang, I., Ramos, R., Kuan, C. H., . . . Nie, Q. (2021). Inference and
574 analysis of cell-cell communication using CellChat. *Nat Commun, 12*(1), 1088.
575 doi:10.1038/s41467-021-21246-9
576 Joost, S., Annusver, K., Jacob, T., Sun, X., Dalessandri, T., Sivan, U., . . . Kasper, M. (2020). The Molecular
577 Anatomy of Mouse Skin during Hair Growth and Rest. *Cell Stem Cell, 26*(3), 441-457 e447.
578 doi:10.1016/j.stem.2020.01.012
579 Kaplan, D. H., Igyarto, B. Z., & Gaspari, A. A. (2012). Early immune events in the induction of allergic contact

580 dermatitis. *Nat Rev Immunol, 12*(2), 114-124. doi:10.1038/nri3150

581 Karsak, M., Gaffal, E., Date, R., Wang-Eckhardt, L., Rehnelt, J., Petrosino, S., . . . Zimmer, A. (2007).
582 Attenuation of allergic contact dermatitis through the endocannabinoid system. *Science, 316*(5830),
583 1494-1497. doi:10.1126/science.1142265

584 Kwon, B. (2018). IFN-gamma in tissue-immune homeostasis and antitumor immunity. *Cell Mol Immunol, 15*(5),
585 531-532. doi:10.1038/cmi.2017.95

586 Laouini, D., Alenius, H., Bryce, P., Oettgen, H., Tsitsikov, E., & Geha, R. S. (2003). IL-10 is critical for Th2
587 responses in a murine model of allergic dermatitis. *J Clin Invest, 112*(7), 1058-1066.
588 doi:10.1172/JCI18246

589 Lefevre, M. A., Nosbaum, A., Rozieres, A., Lenief, V., Mosnier, A., Cortial, A., . . . Vocanson, M. (2021). Unique
590 molecular signatures typify skin inflammation induced by chemical allergens and irritants. *Allergy,*
591 *76*(12), 3697-3712. doi:10.1111/all.14989

592 Liu, Z., Fan, Z., Liu, J., Wang, J., Xu, M., Li, X., . . . Zhang, Z. (2023). Melittin-Carrying Nanoparticle Suppress T
593 Cell-Driven Immunity in a Murine Allergic Dermatitis Model. *Adv Sci (Weinh), 10*(7), e2204184.
594 doi:10.1002/advs.202204184

595 Lynch, M. D., & Watt, F. M. (2018). Fibroblast heterogeneity: implications for human disease. *Journal of Clinical*
596 *Investigation, 128*(1), 26-35. doi:10.1172/JCI93555

597 Manresa, M. C. (2021). Animal Models of Contact Dermatitis: 2,4-Dinitrofluorobenzene-Induced Contact
598 Hypersensitivity. *Methods Mol Biol, 2223*, 87-100. doi:10.1007/978-1-0716-1001-5_7

599 McWhorter, F. Y., Wang, T., Nguyen, P., Chung, T., & Liu, W. F. (2013). Modulation of macrophage phenotype
600 by cell shape. *Proc Natl Acad Sci U S A, 110*(43), 17253-17258. doi:10.1073/pnas.1308887110

601 Meller, S., Lauerma, A. I., Kopp, F. M., Winterberg, F., Anthoni, M., Muller, A., . . . Homey, B. (2007).

602 Chemokine responses distinguish chemical-induced allergic from irritant skin inflammation: memory T
603 cells make the difference. *J Allergy Clin Immunol, 119*(6), 1470-1480. doi:10.1016/j.jaci.2006.12.654
604 Miyake, K., & Karasuyama, H. (2017). Emerging roles of basophils in allergic inflammation. *Allergol Int, 66*(3),
605 382-391. doi:10.1016/j.alit.2017.04.007
606 Miyake, T., Egawa, G., Chow, Z., Asahina, R., Otsuka, M., Nakajima, S., . . . Kabashima, K. (2022). Circadian
607 rhythm affects the magnitude of contact hypersensitivity response in mice. *Allergy, 77*(9), 2748-2759.
608 doi:10.1111/all.15314
609 Moore, M. J., Blachere, N. E., Fak, J. J., Park, C. Y., Sawicka, K., Parveen, S., . . . Darnell, R. B. (2018). ZFP36
610 RNA-binding proteins restrain T cell activation and anti-viral immunity. *Elife, 7*.
611 doi:10.7554/eLife.33057
612 Munoz-Ruiz, M., Llorian, M., D'Antuono, R., Pavlova, A., Mavrigiannaki, A. M., McKenzie, D., . . . Hayday, A. C.
613 (2023). IFN-gamma-dependent interactions between tissue-intrinsic gammadelta T cells and
614 tissue-infiltrating CD8 T cells limit allergic contact dermatitis. *J Allergy Clin Immunol*.
615 doi:10.1016/j.jaci.2023.07.015
616 Plikus, M. V., Wang, X., Sinha, S., Forte, E., Thompson, S. M., Herzog, E. L., . . . Horsley, V. (2021).
617 Fibroblasts: Origins, definitions, and functions in health and disease. *Cell, 184*(15), 3852-3872.
618 doi:10.1016/j.cell.2021.06.024
619 Pollard, K. M., Cauvi, D. M., Toomey, C. B., Morris, K. V., & Kono, D. H. (2013). Interferon-gamma and
620 systemic autoimmunity. *Discov Med, 16*(87), 123-131. Retrieved from
621 https://www.ncbi.nlm.nih.gov/pubmed/23998448
622 Rahman, K., Vengrenyuk, Y., Ramsey, S. A., Vila, N. R., Girgis, N. M., Liu, J., . . . Fisher, E. A. (2017).
623 Inflammatory Ly6Chi monocytes and their conversion to M2 macrophages drive atherosclerosis

624 regression. *J Clin Invest, 127*(8), 2904-2915. doi:10.1172/JCI75005

625 Russell-Goldman, E., & Murphy, G. F. (2020). The Pathobiology of Skin Aging: New Insights into an Old
626 Dilemma. *Am J Pathol, 190*(7), 1356-1369. doi:10.1016/j.ajpath.2020.03.007

627 Schwalie, P. C., Dong, H., Zachara, M., Russeil, J., Alpern, D., Akchiche, N., . . . Deplancke, B. (2018). A
628 stromal cell population that inhibits adipogenesis in mammalian fat depots. *Nature, 559*(7712),
629 103-108. doi:10.1038/s41586-018-0226-8

630 Sun, L., Zhang, X., Wu, S., Liu, Y., Guerrero-Juarez, C. F., Liu, W., . . . Zhang, L. J. (2023). Dynamic interplay
631 between IL-1 and WNT pathways in regulating dermal adipocyte lineage cells during skin development
632 and wound regeneration. *Cell Rep, 42*(6), 112647. doi:10.1016/j.celrep.2023.112647

633 Terui, H., Kimura, Y., Fujimura, C., & Aiba, S. (2021). The IL-1 promoter-driven luciferase reporter cell line
634 THP-G1b can efficiently predict skin-sensitising chemicals. *Arch Toxicol, 95*(5), 1647-1657.
635 doi:10.1007/s00204-021-03022-2

636 Vocanson, M., Hennino, A., Cluzel-Tailhardat, M., Saint-Mezard, P., Benetiere, J., Chavagnac, C., . . . Nicolas,
637 J. F. (2006). CD8+ T cells are effector cells of contact dermatitis to common skin allergens in mice. *J*
638 *Invest Dermatol, 126*(4), 815-820. doi:10.1038/sj.jid.5700174

639 Vocanson, M., Hennino, A., Rozieres, A., Poyet, G., & Nicolas, J. F. (2009). Effector and regulatory
640 mechanisms in allergic contact dermatitis. *Allergy, 64*(12), 1699-1714.
641 doi:10.1111/j.1398-9995.2009.02082.x

642 Wakabayashi, T., Hu, D. L., Tagawa, Y., Sekikawa, K., Iwakura, Y., Hanada, K., & Nakane, A. (2005).
643 IFN-gamma and TNF-alpha are involved in urushiol-induced contact hypersensitivity in mice. *Immunol*
644 *Cell Biol, 83*(1), 18-24. doi:10.1111/j.1440-1711.2005.01310.x

645 Wisgrill, L., Werner, P., Jalonen, E., Berger, A., Lauerma, A., Alenius, H., & Fyhrquist, N. (2021). Integrative

646 transcriptome analysis deciphers mechanisms of nickel contact dermatitis. *Allergy, 76*(3), 804-815.
647 doi:10.1111/all.14519
648 Wongchang, T., Pluangnooch, P., Hongeng, S., Wongkajornsilp, A., Thumkeo, D., & Soontrapa, K. (2023).
649 Inhibition of DYRK1B suppresses inflammation in allergic contact dermatitis model and Th1/Th17
650 immune response. *Sci Rep, 13*(1), 7058. doi:10.1038/s41598-023-34211-x
651 Wu, X., Qi, X., Wang, J., Zhang, Y., Xiao, Y., Tu, C., & Wang, A. (2021). Paeoniflorin attenuates the allergic
652 contact dermatitis response via inhibiting the IFN-gamma production and the
653 NF-kappaB/IkappaBalpha signaling pathway in T lymphocytes. *Int Immunopharmacol, 96*, 107687.
654 doi:10.1016/j.intimp.2021.107687
655 Xiao, G., Deng, A., Liu, H., Ge, G., & Liu, X. (2012). Activator protein 1 suppresses antitumor T-cell function via
656 the induction of programmed death 1. *Proc Natl Acad Sci U S A, 109*(38), 15419-15424.
657 doi:10.1073/pnas.1206370109
658 Xu, Z., Chen, D., Hu, Y., Jiang, K., Huang, H., Du, Y., . . . Chen, T. (2022). Anatomically distinct fibroblast
659 subsets determine skin autoimmune patterns. *Nature, 601*(7891), 118-124.
660 doi:10.1038/s41586-021-04221-8
661 Zachara, M., Rainer, P. Y., Hashimi, H., Russeil, J. M., Alpern, D., Ferrero, R., . . . Deplancke, B. (2022).
662 Mammalian adipogenesis regulator (Areg) cells use retinoic acid signalling to be non- and
663 anti-adipogenic in age-dependent manner. *EMBO J, 41*(18), e108206. doi:10.15252/embj.2021108206
664 Zhang, L. J., Chen, S. X., Guerrero-Juarez, C. F., Li, F., Tong, Y., Liang, Y., . . . Gallo, R. L. (2019).
665 Age-Related Loss of Innate Immune Antimicrobial Function of Dermal Fat Is Mediated by Transforming
666 Growth Factor Beta. *Immunity, 50*(1), 121-136 e125. doi:10.1016/j.immuni.2018.11.003
667 Zhang, L. J., Guerrero-Juarez, C. F., Chen, S. X., Zhang, X., Yin, M., Li, F., . . . Gallo, R. L. (2021).

Diet-induced obesity promotes infection by impairment of the innate antimicrobial defense function of dermal adipocyte progenitors. *Sci Transl Med, 13*(577). doi:10.1126/scitranslmed.abb5280

Zhang, L. J., Guerrero-Juarez, C. F., Hata, T., Bapat, S. P., Ramos, R., Plikus, M. V., & Gallo, R. L. (2015). Innate immunity. Dermal adipocytes protect against invasive Staphylococcus aureus skin infection. *Science, 347*(6217), 67-71. doi:10.1126/science.1260972

Figure legends

Figure 1. Characterization of mouse allergic skin immune response by single cell RNA transcriptomic analysis

(**A**) Overview of the experimental setting. Allergic contact dermatitis (ACD)-like skin inflammation was triggered by sequential sensitization and elicitation of ACD by topical application of 1% or 0.2% DNFB on dorsal or ear skin as indicated. Ear skin was collected at 60 hours post-elicitation for analyses.

(**B**) tSNE plots showing the distribution of various cell clusters marked by a color code.

(**C**) Bubble plots showing the expression of marker genes for each cell cluster. Abbreviations: *dFB*, dermal fibroblast; *MC*, mast cell; *MAC*, macrophage; *BF*, basophil; *NEU*, neutrophil; *VSMC*, vascular smooth muscle cell; *PC*, pericytes; *KC*, keratinocyte; *EC*, endothelial cell; *SC*, Schwann cell.

(**D**) tSNE plots showing how cells were differentially distributed in control and ACD skin samples. Red lines circle key immune cell populations.

(**E**) Stacked bar graph showing the percentage of each cell cluster in the control and ACD samples.

(**F**) qRT-PCR analysis showing the expression of indicated genes (n=4~6/group).

(**G**) Violin plots showing the expression of indicated genes in the control and ACD samples.

Figure supplement 1. Establishment of the DNFB-elicited ACD mouse model.

Figure 2. T cells are primarily polarized to the IFNγ-producing type-1 inflammatory phenotype in ACD

(**A**) tSNE plots showing cell distribution of the $CD45^+CD3^+$ or $THY1^+$ T cell population after re-clustering.

(**B**) Bar graphs showing the percentage of each T cell sub-cluster in the control and the ACD samples.

(**C**) tSNE plots showing cell distribution or the expression of *Ifng* in the control and the ACD samples.

(**D**) By sample violin plots showing the expression of indicated genes across various T cell sub-clusters..

(**E**) WIKI pathway analysis showing the top upregulated (red) or downregulated (blue) pathways in $CD4^+$ and $CD8^+$ T cells in ACD compared to control skin.

(**F**) Volcano plot showing differentially expressed genes in control and ACD samples within the $CD4^+$ and $CD8^+$ T cells

(**G-J**) FACS plots and/or quantified bar graphs showing the percentage of $CD4^+$ or $CD8^+$ T cells (upper panel in G), or the percentage of $IFN\gamma^+IL4/13^-$, $IFN\gamma^-IL4/13^+$, or $IFN\gamma^-IL17A^+$ cells in $CD8^+$ (middle panel in G) and $CD4^+$ (lower panel in G) T cells in control, ACD (24 hours) and ACD (60 hours) ear skin samples (n=3/group).

All error bars indicate mean ± SEM. *$p < 0.05$, **$p < 0.01$, ***$p < 0.001$, ****$p < 0.0001$, ns, non-significant**.**

Figure supplement 1. Characterization of T cell activation in ACD.

Figure 3. Characterization of myeloid cell activation in ACD

(**A**) Stacked bar graphs showing the percentage of indicated myeloid cell populations in the control and

the ACD samples.

(**B**) Violin plots showing the expression of indicated genes across major skin resident and immune cells as indicated.

(**X**) Gene expression plot showing differentially expressed genes in basophils (BF, blue dots) and mast cells (MC, red dots) within the ACD sample.

(**D**) qRT-PCR analysis of indicated genes in ear skin samples (n=3/group).

(**E-F**) FACS plots (**E**) and quantified bar graphs (**F**) showing the percentage of IL4/13^{+} mast cells or basophils within all viable cells in ear skin samples**.**

(**G**) qRT-PCR analysis of indicated genes in ear skin samples (n=3/group).

(**H**) Gene expression plot showing differentially expressed genes in control and ACD samples within the macrophage cell cluster.

(**I**) GO pathway analysis of the upregulated genes (red) or downregulated genes (blue) in macrophage population after ACD elicitation.

(**J-L**) FACS plots (**J**) and quantified bar graphs (**K-L**) showing the percentage of CD11B^{+}Ly6G^{+} neutrophils (NEU) in all cells (**K**), or the percentage of Ly6C^{+} or Ly6C^{-} cells within CD11B^{+}F4/80^{+} macrophages (**L)** in ear skin samples. Unstained (UN) plot was shown as negative gating control. All error bars indicate mean ± SEM. *p < 0.05, **p < 0.01, ***p < 0.001, ****p < 0.0001, ns, non-significant.

Figure supplement 1. Analysis of myeloid cell activation in ACD

Figure 4. Characterization of the immune response of dermal fibroblasts in ACD

(**A**) tSNE plots showing cell distribution of the Pdgfra^{+} dermal fibroblasts after re-clustering.

(**B**) Bubble plots showing the expression of marker genes for each dFB cell cluster. Abbreviations: AP, adipocyte progenitors; Areg, adipogenesis-regulatory cells; pAd, preadipocytes; RET/PAP, reticular and/or papillary dFBs; pF, peri-follicular dFBs.

(**C**) Violin plots showing the expression of indicated genes across various dFB sub-populations in the control and the ACD samples.

(**D**) SCENIC analysis showing the top enriched transcriptional factors in various dFB clusters.

(**E**) GO pathway analysis of the upregulated genes (red) or downregulated genes (blue) in the r5 dFB cluster after ACD elicitation.

(**F**) Volcano plot showing differentially expressed genes in control and ACD samples within the r5 dFB cluster.

(**G**) Violin plots showing the expression of indicated genes across various cell populations in the control and the ACD samples.

(**H**) Frozen sections of control and ACD ear skin samples were subjected to immunostaining analysis using antibodies against CXCL9 (green) and PDGFRA (red). Nuclei were counter stained by DAPI (blue). Dermal CXCL9^{+} or PDGFRA^{-} cells were highlighted by either red- or green-dotted lines in the zoom-in panel. Scale bar, 200 μm. Zoom-in image is shown on the right-hand side.

(**I-J**) Quantified results showing the fluorescent intensity (arbitrary unit, AU) of CXCL9, CXCL10 or PDGFRA in the dermal CXCL9/10^{+} cells or PDGFRA^{-} cells shown in Fig. 4H or Fig. S4G.

All error bars indicate mean ± SEM. *$p < 0.05$, ***$p < 0.001$, ****$p < 0.0001$, ns, non-significant.

Figure supplement 1. Characterization of the immune response of dermal fibroblasts in ACD.

Figure 5. Interaction between dFBs and T cells via the IFNG-CXCL10-CXCR3 signaling

axis in ACD

(**A**) Circle plot from cell-chat analysis showing the inferred intercellular communication network for IFNγ-IFNGR signaling in the control and the ACD cells.

(**B-C**) Primary neonatal dFBs were treated with IFNγ, IL4 or IL17A for 48 hours and subjected to RNA-seq analysis. (**B**) Venn diagram comparing genes up-regulated by IFNγ, IL4. (**C**) GO pathway analysis of the genes upregulated only by IFNγ.

(**D**) Primary dFBs were treated with IFNγ for 8h or 48h, and control or IFNγ treated samples were subjected to qRT-PCR analysis of *Cxcl9, Cxcl10, Stat1, Apoe,* and *Col1a1* mRNA expression (n=~3/group).

(**E**-**H**) **E:** Experiment scheme for collection of IFNγ-primed dFB conditioned medium ($dFB^{IFNγ}$-CM) or control dFB^{ctrl}-CM to stimulate naïve T cells. **F:** ELISA analysis showing protein levels of CXCL10 in dFB^{ctrl}-CM and $dFB^{IFNγ}$-CM. **G**-**H:** Naïve T lymphocytes stimulated without (**G**) or with CD3/28-Ab (**H**) were treated with dFB^{ctrl}-CM or $dFB^{IFNγ}$-CM with or w/o CXCR3 neutralizing antibody, and cell supernatants were collected for ELISA analysis of IFNγ protein expression.

All error bars indicate mean ± SEM. *p < 0.05, **p < 0.01,***p < 0.001, ****p < 0.0001, ns, non-significant.

Figure supplement 1. Interaction between dFBs and T cells via the IFNG-CXCL10-CXCR3 signaling axis in ACD.

Figure 6. Targeted deletion of Ifngr in dFBs inhibited the development of type-1 skin inflammation in ACD

(**A**) Tamoxifen-inducible targeted deletion of *Ifngr1* in $PDGFRA^{+}$ fibroblasts (*Ifngr1*$^{FB\text{-}iKO}$) was achieved by crossing *Ifngr1*$^{f/f}$ and *Pdgfra*-cre/*ERT* mice, and mice were subjected to DNFB-induced ACD model as

indicated.

(**B**) Multiplex-PCR based genotyping using allele specific primers yields DNA products having sizes specific for the wild-type and Ifngr1-floxed alleles. Lower gel shows gene products for Cre and/or internal product control (IPC) as indicated.

(**C**) Skin samples were immunostained with IFNGR1 (green) and PDGFRA (blue), and nuclei were counterstained with DAPI (white). Scale, 100 μm.

(**D-E**) Representative ear skin images (**D**) for each group at 60 hours after ACD elicitation. Br graphs (**E**) showing quantified Eczema Area and Severity Index (EASI) scores for each group (n=6~12 /group).

(**F**) H&E staining of skin sections for each group at 60 hours after ACD elicitation

(**G**) qRT-PCR analysis of the mRNA expression levels of indicated genes (ratios to HK gene *Tbp* were shown, n=3~8/group).

(**H-I**) Immunostaining (**H**) of skin sections with anti-CD8 (red) and anti-PDGFRA (blue) antibodies, and nuclei were counter stained by DAPI (white). Zoom-in images were shown in the lower panel. Quantified results (**I**) showing the # of $CD8^+$ T cells per $1mm^2$ of dermal area in ACD skin.

All error bars indicate mean ± SEM. *$p < 0.05$, **$p < 0.01$,***$p < 0.001$, ****$p < 0.0001$.

Figure supplement 1. Targeted deletion of *Ifngr1* in dFBs inhibited the development of type-1 skin inflammation in ACD.

Figure 7. Activation of dermal T cells and fibroblasts in human ACD skin samples

(**A**) Skin sections from healthy control (HC) or ACD human skin samples were immunostained with antibodies against CD4 (green), CD8 (blue) and IFNγ (red) (representative of n=3/group). Nuclei were counter stained by DAPI (white). Scale bar, 200 μm. Zoom-in image is shown on the right-hand side.

(**B**) Upper panel is the zoom-in images from Fig. 6A. Lower panel is the quantified intensity profiles of CD8 (blue) and IFNγ (red) from left to right of the images marked by yellow dashed boxes.

(**C**) Skin sections from healthy control (HC) or ACD human skin samples were subjected to Masson's staining, in which collagen bundles were stained in blue.

(**D**) Skin sections from healthy control (HC) or ACD human skin samples were immunostained with antibodies against CD8 (red) and PDGFRA (blue), and representative images of dermal lobular structures were shown (representative of n=3/group).

(**E**) Skin sections from healthy control (HC) or ACD human skin samples were immunostained with CXCL10 (green) and PDGFRA (blue). Nuclei were counter stained by DAPI (white). Scale bar, 200 μm. Zoom-in image is shown on the right-hand side

(**F**) Upper panel is the zoom-in images from Fig. 6E. Lower panel is the quantified intensity profiles of PDGFRA (blue) and CXCL10 (green) from left to right of the images marked by yellow dashed boxes.

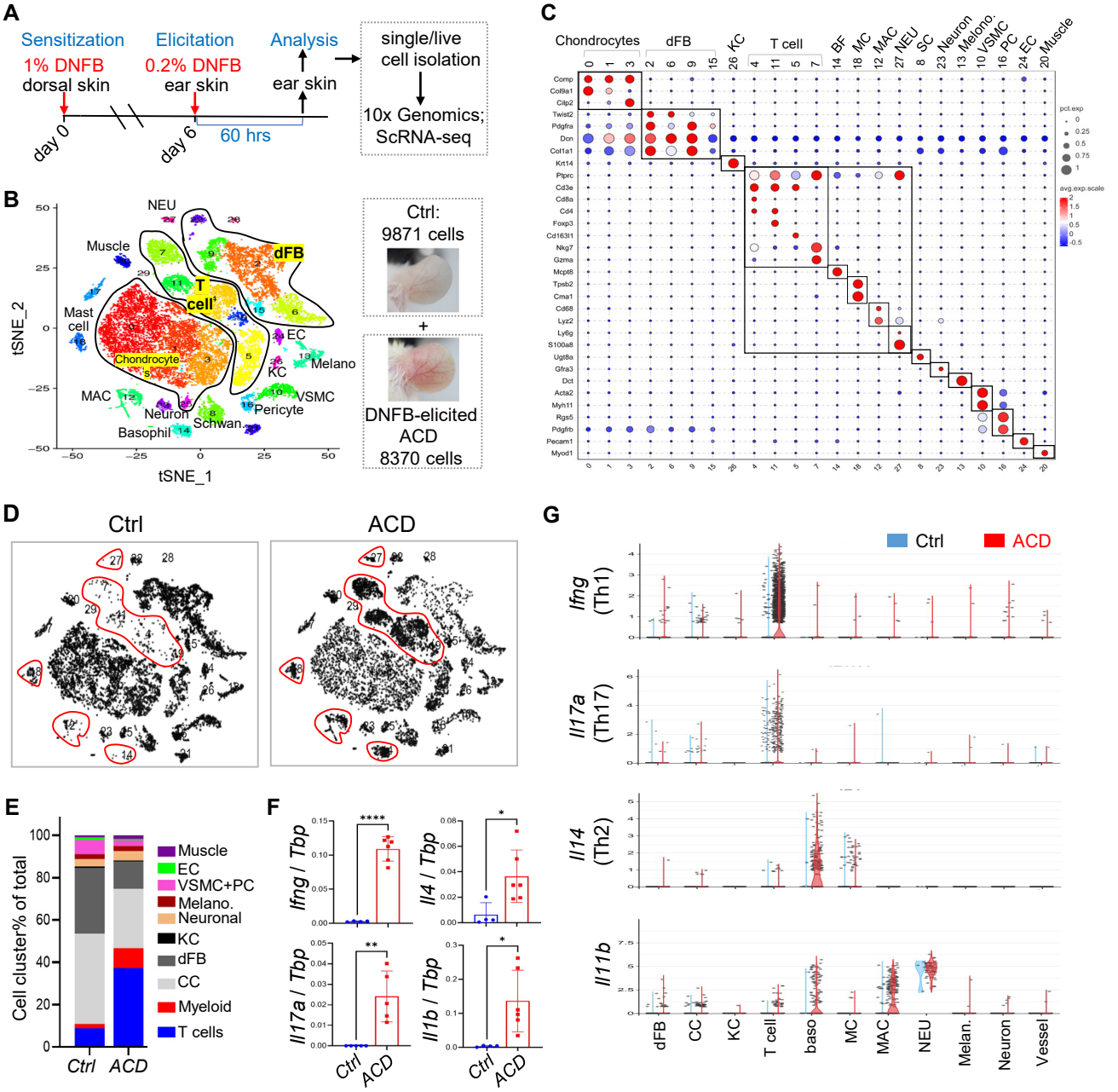
A
Sensitization
1% DNFB
dorsal skin
Elicitation
0.2% DNFB
ear skin
Analysis
ear skin
day 0
day 6
60 hrs
single/live cell isolation
10x Genomics; ScRNA-seq
B
NEU
Muscle
dFB
T cell
Mast cell
Chondrocytes
EC
KC
Melano
MAC
VSMC
Pericyte
Neuron
Schwan.
Basophil
tSNE_2
tSNE_1
Ctrl:
9871 cells
+
DNFB-elicited ACD
8370 cells
C
Chondrocytes
dFB
KC
T cell
BF
MC
MAC
NEU
SC
Neuron
Melono.
VSMC
PC
EC
Muscle
D
Ctrl
ACD
E
Cell cluster-% of total
Muscle
EC
VSMC+PC
Melano.
Neuronal
KC
dFB
CC
Myeloid
T cells
Ctrl
ACD
F
Ifng / Tbp
Il4 / Tbp
Il17a / Tbp
Il1b / Tbp
Ctrl
ACD
G
Ctrl
ACD
Ifng (Th1)
Il17a (Th17)
Il14 (Th2)
Il11b
dFB
CC
KC
T cell
baso
MC
MAC
NEU
Melan.
Neuron
Vessel

Figure 1

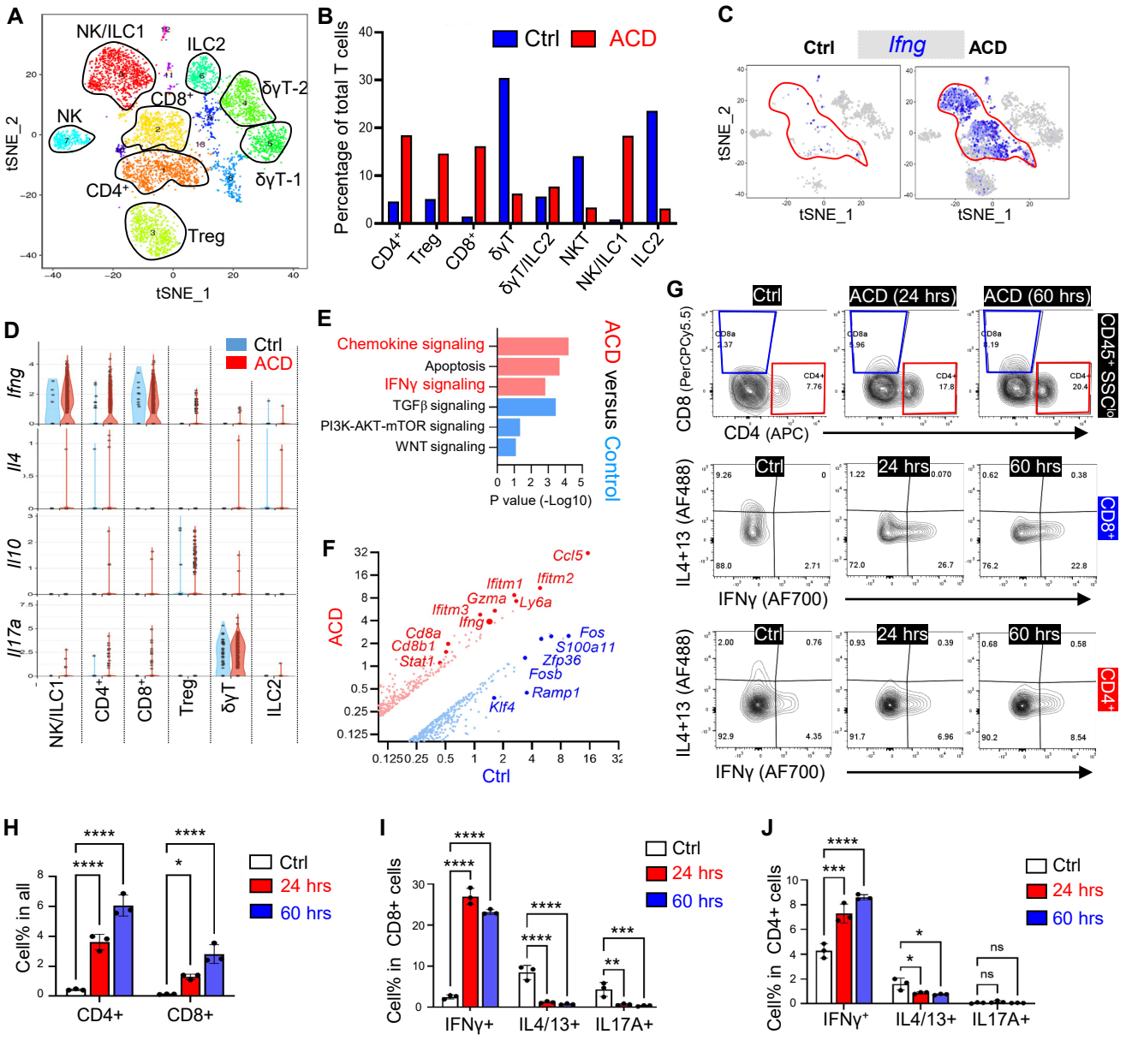
A
NK/ILC1
ILC2
δγT-2
CD8+
NK
δγT-1
CD4+
Treg
tSNE_2
tSNE_1
B
Ctrl
ACD
Percentage of total T cells
CD4+
Treg
CD8+
δγT
δγT/ILC2
NKT
NK/ILC1
ILC2
C
Ctrl
Ifng
ACD
tSNE_2
tSNE_1
D
Ctrl
ACD
Ifng
Il4
Il10
Il17a
NK/ILC1
CD4+
CD8+
Treg
δγT
ILC2
E
Chemokine signaling
Apoptosis
IFNγ signaling
TGFβ signaling
PI3K-AKT-mTOR signaling
WNT signaling
P value (-Log10)
ACD versus Control
F
ACD
Ctrl
Ccl5
Ifitm1
Ifitm2
Gzma
Ly6a
Ifitm3
Ifng
Cd8a
Cd8b1
Stat1
Fos
S100a11
Zfp36
Fosb
Ramp1
Klf4
G
Ctrl
ACD (24 hrs)
ACD (60 hrs)
CD8 (PerCPCy5.5)
CD4 (APC)
CD45+ SSClo
24 hrs
60 hrs
CD8+
CD4+
IL4+13 (AF488)
IFNγ (AF700)
H
Cell% in all
CD4+
CD8+
Ctrl
24 hrs
60 hrs
I
Cell% in CD8+ cells
IFNγ+
IL4/13+
IL17A+
J
Cell% in CD4+ cells
IFNγ+
IL4/13+
IL17A+
ns

Figure 2

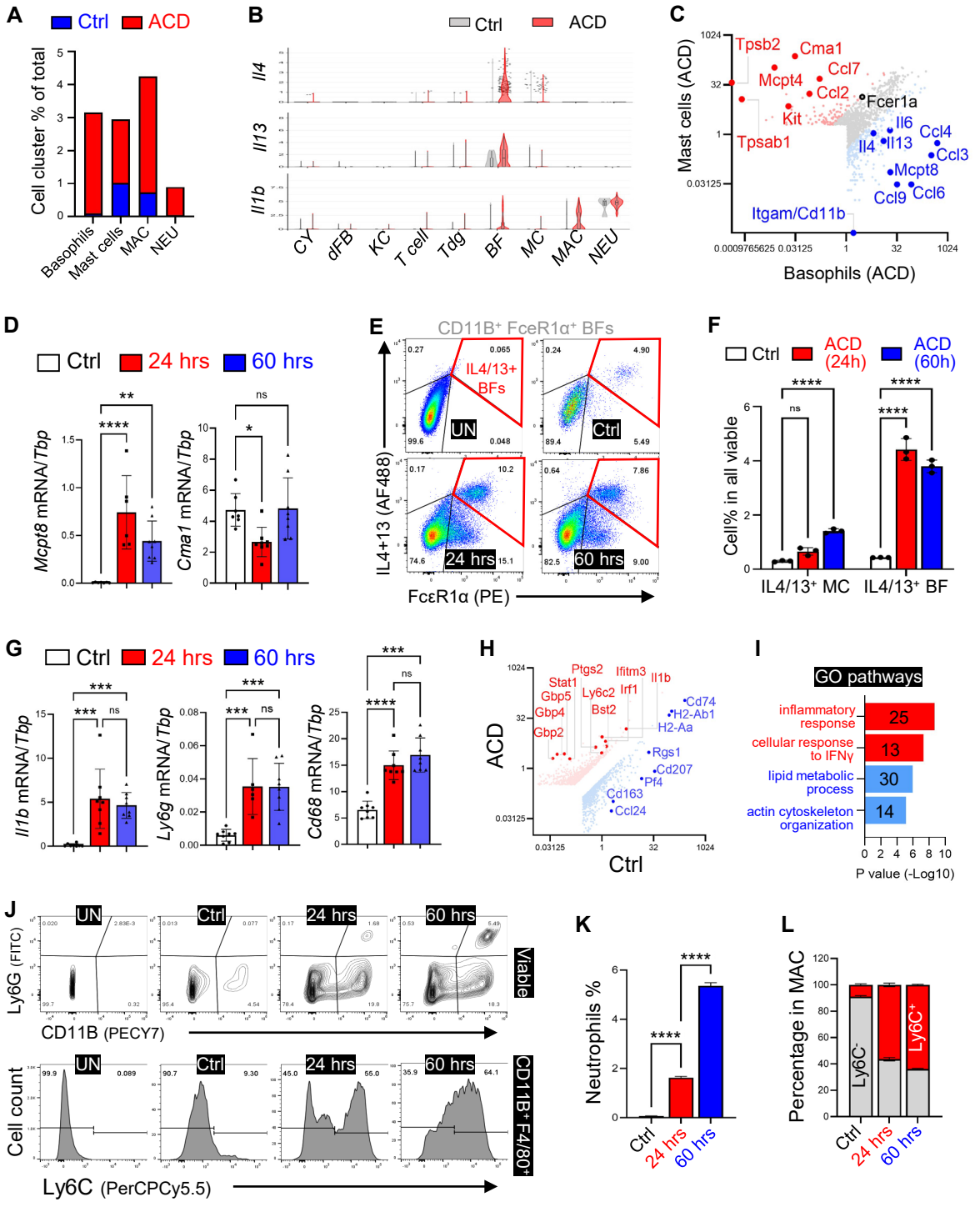
A
Ctrl
ACD
Cell cluster % of total
Basophils
Mast cells
MAC
NEU
B
Ctrl
ACD
Il4
Il13
Il1b
CY
dFB
KC
T cell
Tdg
BF
MC
MAC
NEU
C
Mast cells (ACD)
Basophils (ACD)
Tpsb2
Cma1
Ccl7
Mcpt4
Ccl2
Fcer1a
Kit
Tpsab1
Il6
Ccl4
Il4
Il13
Ccl3
Mcpt8
Ccl9
Ccl6
Itgam/Cd11b
D
Ctrl
24 hrs
60 hrs
Mcpt8 mRNA/Tbp
Cma1 mRNA/Tbp
E
CD11B+ FceR1α+ BFs
IL4/13+ BFs
UN
Ctrl
24 hrs
60 hrs
IL4+13 (AF488)
FcεR1α (PE)
F
Ctrl
ACD (24h)
ACD (60h)
Cell% in all viable
IL4/13+ MC
IL4/13+ BF
G
Ctrl
24 hrs
60 hrs
Il1b mRNA/Tbp
Ly6g mRNA/Tbp
Cd68 mRNA/Tbp
H
ACD
Ctrl
Ptgs2
Ifitm3
Il1b
Stat1
Gbp5
Ly6c2
Irf1
Gbp4
Bst2
Gbp2
Cd74
H2-Ab1
H2-Aa
Rgs1
Cd207
Pf4
Cd163
Ccl24
I
GO pathways
inflammatory response
25
cellular response to IFNγ
13
lipid metabolic process
30
actin cytoskeleton organization
14
P value (-Log10)
J
UN
Ctrl
24 hrs
60 hrs
Viable
Ly6G (FITC)
CD11B (PECY7)
Cell count
CD11B+F4/80+
Ly6C (PerCPCy5.5)
K
Neutrophils %
Ctrl
24 hrs
60 hrs
L
Percentage in MAC
Ly6C-
Ly6C+
Ctrl
24 hrs
60 hrs

Figure 3

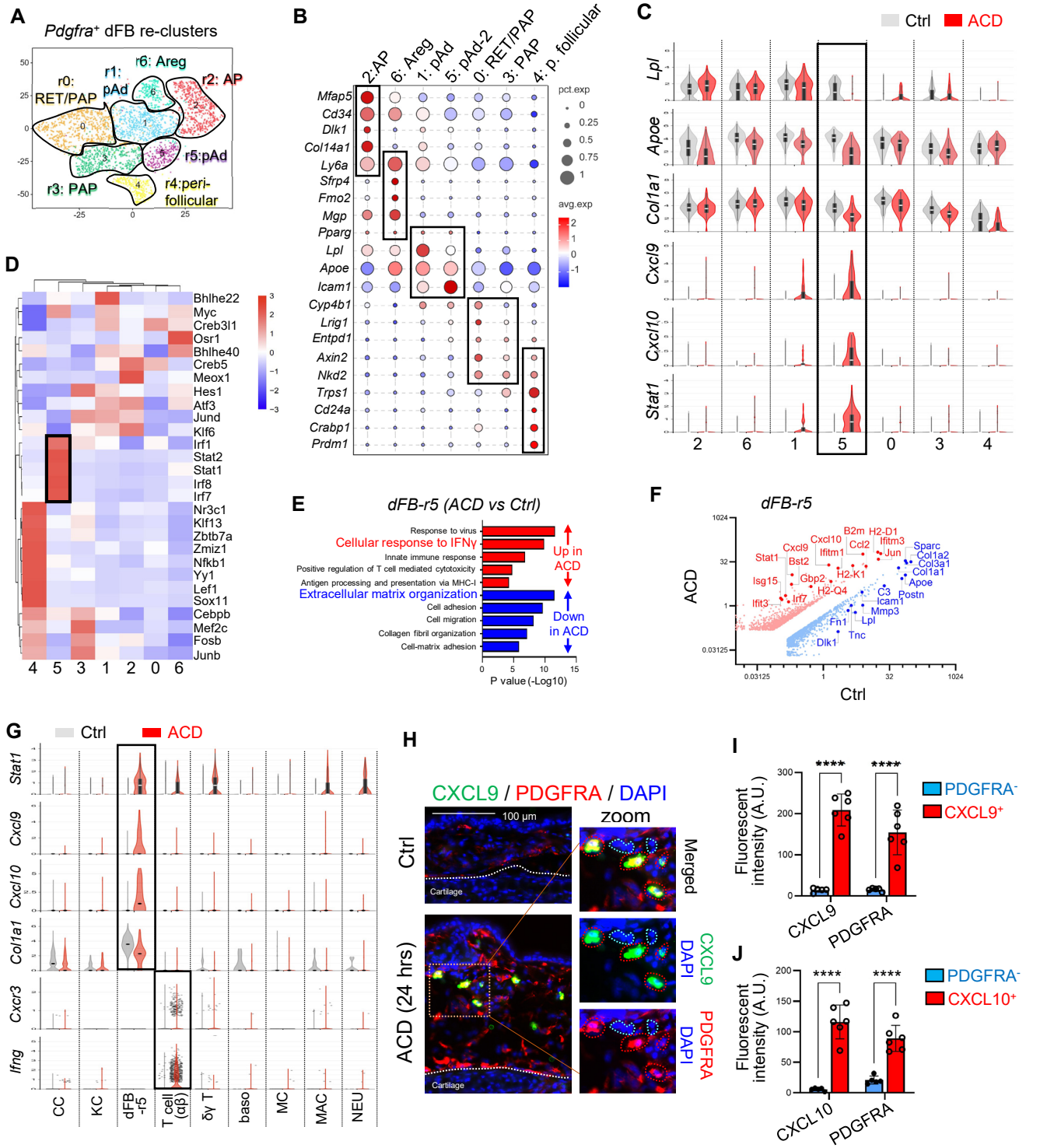
A
Pdgfra+ dFB re-clusters
r0: RET/PAP
r1: pAd
r6: Areg
r2: AP
r5:pAd
r3: PAP
r4:peri-follicular
B
2:AP
6: Areg
1: pAd
5: pAd-2
0: RET/PAP
3: PAP
4: p. follicular
Mfap5
Cd34
Dlk1
Col14a1
Ly6a
Sfrp4
Fmo2
Mgp
Pparg
Lpl
Apoe
Icam1
Cyp4b1
Lrig1
Entpd1
Axin2
Nkd2
Trps1
Cd24a
Crabp1
Prdm1
pct.exp
avg.exp
C
Ctrl
ACD
Lpl
Apoe
Col1a1
Cxcl9
Cxcl10
Stat1
D
Bhlhe22
Myc
Creb3l1
Osr1
Bhlhe40
Creb5
Meox1
Hes1
Atf3
Jund
Klf6
Irf1
Stat2
Stat1
Irf8
Irf7
Nr3c1
Klf13
Zbtb7a
Zmiz1
Nfkb1
Yy1
Lef1
Sox11
Cebpb
Mef2c
Fosb
Junb
E
dFB-r5 (ACD vs Ctrl)
Response to virus
Cellular response to IFNγ
Innate immune response
Positive regulation of T cell mediated cytotoxicity
Antigen processing and presentation via MHC-I
Extracellular matrix organization
Cell adhesion
Cell migration
Collagen fibril organization
Cell-matrix adhesion
Up in ACD
Down in ACD
P value (-Log10)
F
dFB-r5
ACD
Ctrl
G
Ctrl
ACD
Stat1
Cxcl9
Cxcl10
Col1a1
Cxcr3
Ifng
CC
KC
dFB -r5
T cell (αβ)
δγ T
baso
MC
MAC
NEU
H
CXCL9 / PDGFRA / DAPI
100 µm
zoom
Ctrl
ACD (24 hrs)
Merged
CXCL9 DAPI
PDGFRA DAPI
Cartilage
I
Fluorescent intensity (A.U.)
PDGFRA-
CXCL9+
CXCL9
PDGFRA
J
PDGFRA-
CXCL10+
CXCL10
PDGFRA

Figure 4

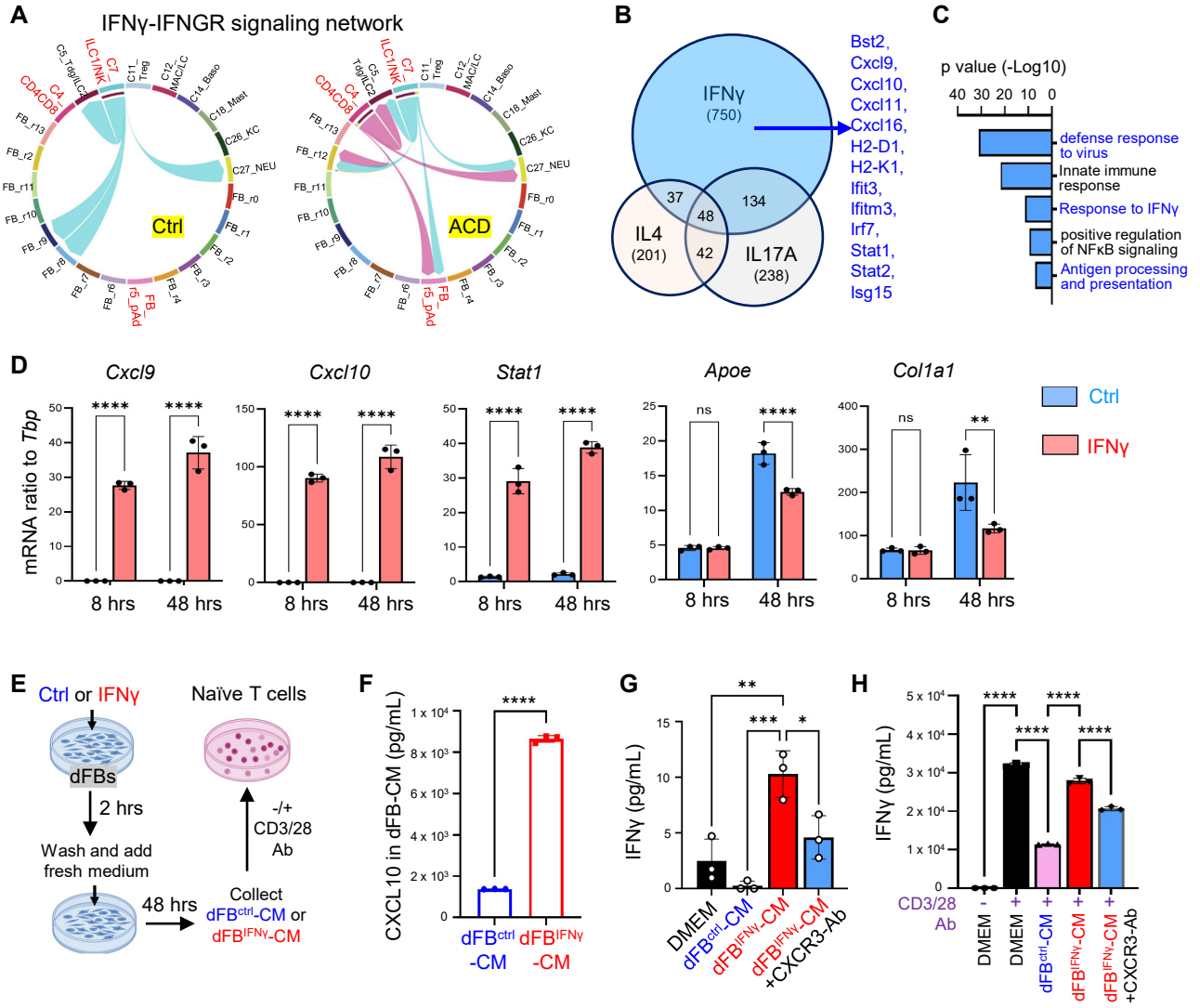
A
IFNγ-IFNGR signaling network
Ctrl
ACD
B
IFNγ
(750)
IL4
(201)
IL17A
(238)
37
48
134
42
Bst2,
Cxcl9,
Cxcl10,
Cxcl11,
Cxcl16,
H2-D1,
H2-K1,
Ifit3,
Ifitm3,
Irf7,
Stat1,
Stat2,
Isg15
C
p value (-Log10)
40 30 20 10 0
defense response to virus
Innate immune response
Response to IFNγ
positive regulation of NFκB signaling
Antigen processing and presentation
D
Cxcl9
Cxcl10
Stat1
Apoe
Col1a1
mRNA ratio to Tbp
8 hrs
48 hrs
Ctrl
IFNγ
E
Ctrl or IFNγ
dFBs
2 hrs
Wash and add fresh medium
48 hrs
Collect dFBctrl-CM or dFBIFNγ-CM
Naïve T cells
-/+ CD3/28 Ab
F
CXCL10 in dFB-CM (pg/mL)
dFBctrl -CM
dFBIFNγ -CM
G
IFNγ (pg/mL)
DMEM
dFBctrl-CM
dFBIFNγ-CM
dFBIFNγ-CM +CXCR3-Ab
H
IFNγ (pg/mL)
CD3/28 Ab
DMEM
DMEM
dFBctrl-CM
dFBIFNγ-CM
dFBIFNγ-CM +CXCR3-Ab

Figure 5

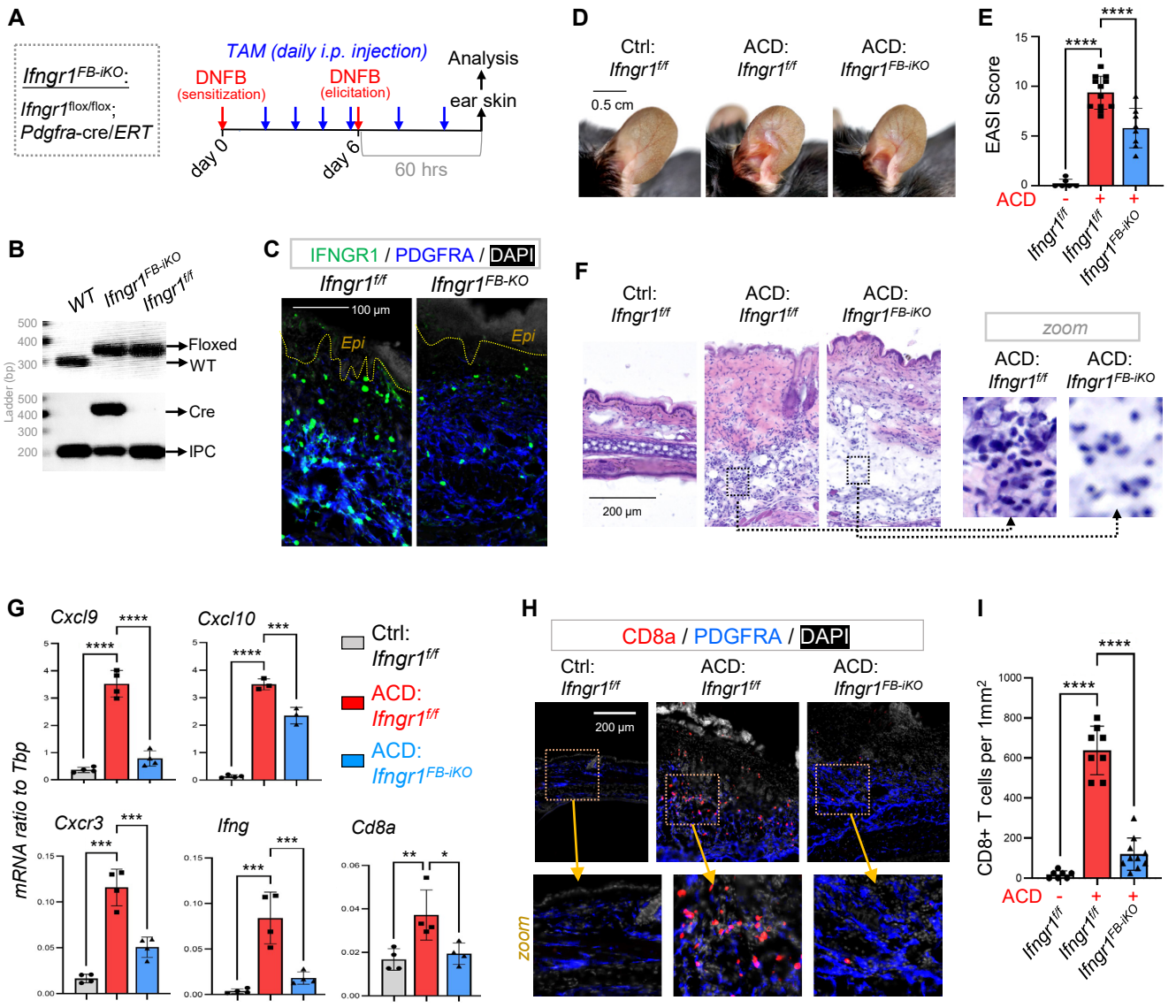
A
Ifngr1FB-iKO:
Ifngr1flox/flox;
Pdgfra-cre/ERT
TAM (daily i.p. injection)
DNFB
(sensitization)
DNFB
(elicitation)
Analysis
ear skin
day 0
day 6
60 hrs
B
WT
Ifngr1FB-iKO
Ifngr1f/f
Floxed
WT
Cre
IPC
Ladder (bp)
C
IFNGR1 / PDGFRA / DAPI
Ifngr1f/f
Ifngr1FB-KO
100 µm
Epi
D
Ctrl: Ifngr1f/f
ACD: Ifngr1f/f
ACD: Ifngr1FB-iKO
0.5 cm
E
EASI Score
ACD
F
Ctrl: Ifngr1f/f
ACD: Ifngr1f/f
ACD: Ifngr1FB-iKO
200 µm
zoom
G
Cxcl9
Cxcl10
Cxcr3
Ifng
Cd8a
mRNA ratio to Tbp
Ctrl: Ifngr1f/f
ACD: Ifngr1f/f
ACD: Ifngr1FB-iKO
H
CD8a / PDGFRA / DAPI
Ctrl: Ifngr1f/f
ACD: Ifngr1f/f
ACD: Ifngr1FB-iKO
200 µm
zoom
I
CD8+ T cells per 1mm2
ACD

Figure 6

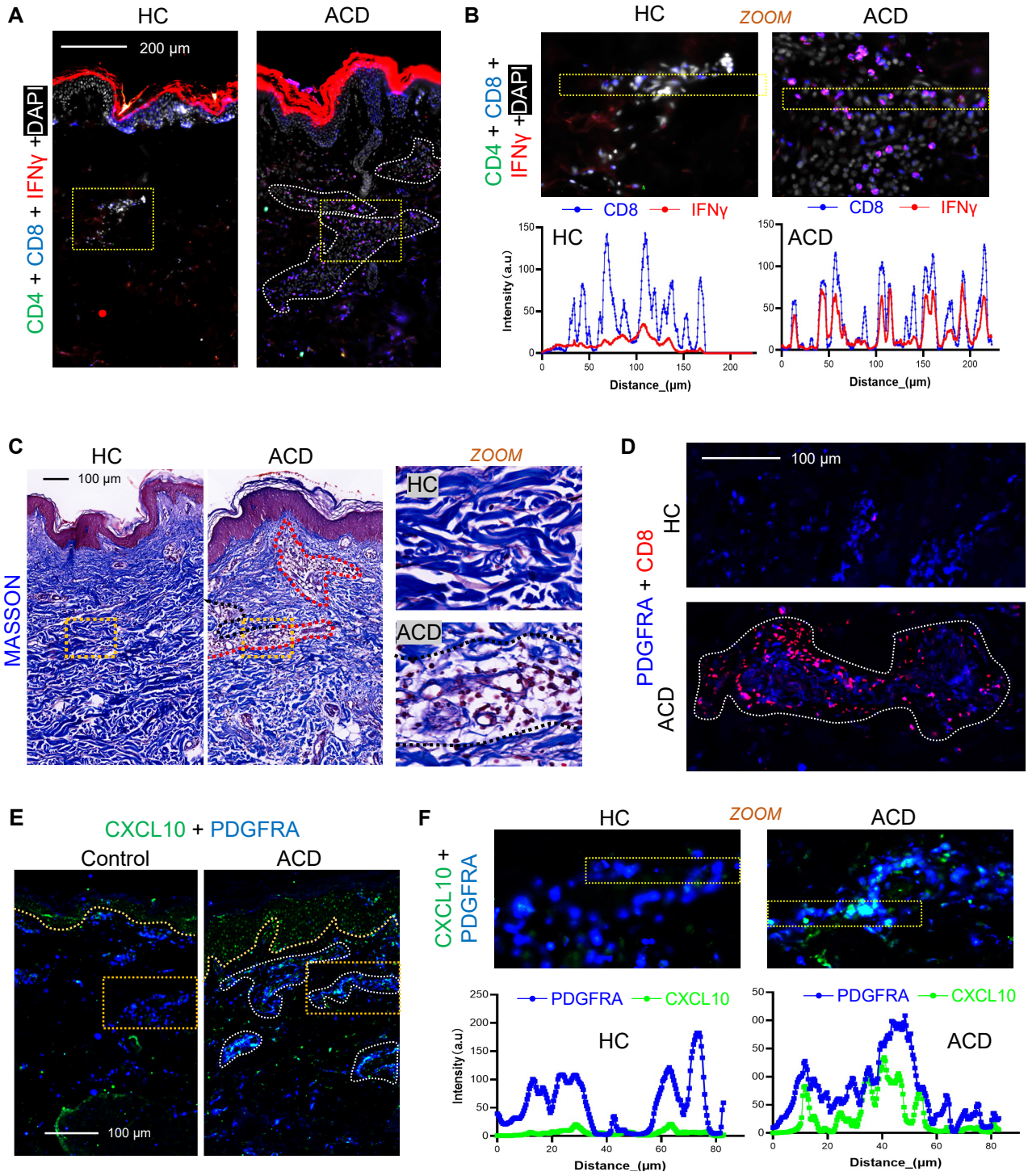
A
HC
ACD
200 µm
CD4 + CD8 + IFNγ +DAPI
B
HC
ZOOM
ACD
CD4 + CD8 + IFNγ +DAPI
CD8
IFNγ
HC
ACD
Intensity (a.u)
Distance_(µm)
C
HC
ACD
ZOOM
100 µm
MASSON
HC
ACD
D
100 µm
PDGFRA + CD8
HC
ACD
E
CXCL10 + PDGFRA
Control
ACD
100 µm
F
HC
ZOOM
ACD
CXCL10 + PDGFRA
PDGFRA
CXCL10
HC
ACD
Intensity (a.u)
Distance_(µm)

Figure 7